

## Article

# CHANG-ES XXXI—A Decade of CHANG-ES: What We Have Learned from Radio Observations of Edge-on Galaxies

Judith Irwin <sup>1,\*</sup> , Rainer Beck <sup>2</sup>, Tanden Cook <sup>1</sup>, Ralf-Jürgen Dettmar <sup>3</sup> , Jayanne English <sup>4</sup> , Volker Heesen <sup>5</sup>, Richard Henriksen <sup>1</sup>, Yan Jiang <sup>6</sup>, Jiang-Tao Li <sup>6</sup> , Li-Yuan Lu <sup>6,7</sup> , Crystal Mele <sup>3</sup>, Ancla Müller <sup>3</sup>, Eric Murphy <sup>8</sup> , Troy Porter <sup>9</sup>, Richard Rand <sup>10</sup>, Nathan Skeggs <sup>1</sup>, Michael Stein <sup>3</sup> , Yelena Stein <sup>3</sup>, Jeroen Stil <sup>11</sup>, Andrew Strong <sup>12</sup> , Rene Walterbos <sup>13</sup> , Q. Daniel Wang <sup>14</sup>, Theresa Wiegert <sup>15</sup>  and Yang Yang <sup>6</sup> 

<sup>1</sup> Department of Physics, Engineering Physics & Astronomy, Queen's University, Kingston, ON K7L 3N6, Canada; tanden.cook@gmail.com (T.C.); henrikr@queensu.ca (R.H.); nathan.skeggs@queensu.ca (N.S.)

<sup>2</sup> Max-Planck-Institut für Radioastronomie, Auf dem Hügel 69, 53121 Bonn, Germany; rbeck@mpifr-bonn.mpg.de

<sup>3</sup> Faculty of Physics and Astronomy, Astronomical Institute (AIRUB), Ruhr University Bochum, 44780 Bochum, Germany; dettmar@astro.rub.de (R.-J.D.); cmele@astro.rub.de (C.M.); amueller@astro.rub.de (A.M.); mstein@astro.rub.de (M.S.); stein@astro.rub.de (Y.S.)

<sup>4</sup> Department of Physics & Astronomy, University of Manitoba, Winnipeg, MB R3T 2N2, Canada; jayanne.english@umanitoba.ca

<sup>5</sup> Hamburg Observatory, Universität Hamburg, Gojenbergsweg 112, 21029 Hamburg, Germany; volker.heesen@hs.uni-hamburg.de

<sup>6</sup> Purple Mountain Observatory, Chinese Academy of Sciences, 10 Yuanhua Road, Nanjing 210023, China; yanjiang@pmo.ac.cn (Y.J.); pandataotao@gmail.com (J.-T.L.); lylu@pmo.ac.cn or luliuyan@stu.xmu.edu.cn (L.-Y.L.); yangyang.astro@gmail.com (Y.Y.)

<sup>7</sup> Department of Astronomy, Xiamen University, 422 Siming South Road, Xiamen 361005, China

<sup>8</sup> National Radio Astronomy Observatory, 520 Edgemont Road, Charlottesville, VA 22903, USA; emurphy@nrao.edu

<sup>9</sup> Kavli Institute for Particle Astrophysics and Cosmology, SLAC, 2575 Sand Hill Road, M/S 29, Menlo Park, CA 94025, USA; tporter@stanford.edu

<sup>10</sup> Department of Physics & Astronomy, University of New Mexico, 210 Yale Blvd. NE, Albuquerque, NM 87106, USA; rjr@phys.unm.edu

<sup>11</sup> Department of Physics and Astronomy, University of Calgary, 2500 University Drive NW, Calgary, AB T2N 1N4, Canada; jstil@ucalgary.ca

<sup>12</sup> Max Planck Institute for Extraterrestrial Physics, Gießenbachstraße 1, 85748 Garching, Germany; aws@mpe.mpg.de

<sup>13</sup> Astronomy Department, New Mexico State University, Las Cruces, NM 88003, USA; rwalterb@nmsu.edu

<sup>14</sup> Department of Astronomy, University of Massachusetts, North Pleasant Street, Amherst, MA 01003-9305, USA; wqd@umass.edu

<sup>15</sup> Departamento Astronomía Extragaláctica, Instituto de Astrofísica de Andalucía (IAA-CSIC), Glorieta de la Astronomía s/n, 18008 Granada, Spain; twiegert@iaa.es

\* Correspondence: irwinja@queensu.ca



**Citation:** Irwin, J.; Beck, R.; Cook, T.; Dettmar, R.-J.; English, J.; Heesen, V.; Henriksen, R.; Jiang, Y.; Li, J.-T.; Lu, L.-Y.; et al. CHANG-ES XXXI—A Decade of CHANG-ES: What We Have Learned from Radio Observations of Edge-on Galaxies. *Galaxies* **2024**, *12*, 22. <https://doi.org/10.3390/galaxies12030022>

Academic Editor: Gisela N. Ortiz-León

Received: 31 March 2024

Revised: 28 April 2024

Accepted: 1 May 2024

Published: 6 May 2024



**Copyright:** © 2024 by the authors. Licensee MDPI, Basel, Switzerland. This article is an open access article distributed under the terms and conditions of the Creative Commons Attribution (CC BY) license (<https://creativecommons.org/licenses/by/4.0/>).

**Abstract:** CHANG-ES (Continuum Halos in Nearby Galaxies—an EVLA Survey) is an ambitious project to target 35 nearby disk galaxies that are edge-on to the line of sight. The orientation permits both the disk and halo regions to be studied. The observations were initially at 1.5 GHz (L-band) and 6.0 GHz (C-band) in a variety of VLA array configurations, and in all four Stokes parameters, which allowed for spatially resolved images in total intensity plus polarization. The inclusion of polarization is unique to an edge-on galaxy survey and reveals the galaxies' halo magnetic fields. This paper will summarize the results to date, some of which are new phenomena, never seen prior to CHANG-ES. For example, we see that 'X-type' fields, as well as rotation measure reversals, are common features of spiral galaxies. Further observations at 3.0 GHz (S-band) as well as future scientific opportunities will also be described.

**Keywords:** galaxies: individual; galaxies: spiral; galaxies: magnetic fields; radio continuum: galaxies

## 1. Introduction

The CHANG-ES (Continuum Halos in Nearby Galaxies—an EVLA Survey) project targets 35 edge-on galaxies in the radio continuum with wide bandwidths centered at 1.6 GHz (L-band) and 6.0 GHz (C-band), using the Karl G. Jansky Very Large Array<sup>1</sup> (hereafter, the VLA). An earlier paper, also published by the Multidisciplinary Digital Publishing Institute (MDPI) has summarized important CHANG-ES results for the year 2019 [1]. In this paper, we further update and highlight some significant CHANG-ES insights and discoveries.

The gaseous halos ( $z \gtrsim 1$  kpc) of galaxies can be interrogated by focusing on systems that are edge-on to the line of sight, where  $z$  is the height above the plane. To this end, we have targeted 35 such galaxies. Our selection criteria were as follows: (1) an inclination  $> 75^\circ$ , as given in the Nearby Galaxies Catalog [2], (2) a declination  $> -23^\circ$  for detectability at the VLA, (3) an optical size between 4 and 15 arcmin (except for NGC 5775) to match VLA array configurations, and (4) flux densities at the L-band of at least 23 mJy (except for NGC 4244) in order for a detection to be likely. It should be noted that the sample does not specify high star formation rates (SFRs) or galaxy type, active galactic nuclei (AGNs), etc.—only that the galaxy has an identifiable disk (i.e., not ellipticals). Consequently, we are targeting ‘normal’ galaxies; for example, SFRs range from 0.06 to 10.5  $M_\odot \text{ yr}^{-1}$  and distances range from 4.4 to 42 Mpc (Table 1).

**Table 1.** CHANG-ES galaxy sample <sup>a</sup>.

Galaxy	Distance <sup>b</sup> Mpc	SFR <sup>c</sup> $M_\odot \text{ yr}^{-1}$
N 660	12.3	$3.31 \pm 0.32$
N 891	9.1	$1.88 \pm 0.18$
N 2613	23.4	$3.36 \pm 0.35$
N 2683	6.27	$0.25 \pm 0.03$
N 2820	26.5	$1.35 \pm 0.14$
N 2992	34	$5.91 \pm 0.54$
N 3003	25.4	$1.56 \pm 0.16$
N 3044	20.3	$1.75 \pm 0.16$
N 3079	20.6	$5.08 \pm 0.45$
N 3432	9.42	$0.51 \pm 0.06$
N 3448	24.5	$1.78 \pm 0.18$
N 3556	14.09	$3.57 \pm 0.30$
N 3628	8.5	$1.41 \pm 0.12$
N 3735	42	$6.23 \pm 0.57$
N 3877	17.7	$1.35 \pm 0.12$
N 4013	16	$0.71 \pm 0.07$
N 4096	10.32	$0.71 \pm 0.08$
N 4157	15.6	$1.76 \pm 0.18$
N 4192	13.55	$0.78 \pm 0.07$
N 4217	20.6	$1.89 \pm 0.18$
N 4244	4.4	$0.06 \pm 0.01$
N 4302	19.41	$0.92 \pm 0.08$
N 4388	16.6	$2.42 \pm 0.23$
N 4438 <sup>d</sup>	10.39	$0.14 \pm 0.04$
N 4565	11.9	$0.96 \pm 0.09$
N 4594	12.7	$0.43 \pm 0.04$
N 4631	7.4	$2.62 \pm 0.22$
N 4666	27.5	$10.5 \pm 0.92$
N 4845	16.98	$0.62 \pm 0.06$
N 5084 <sup>e</sup>	23.4	$0.12 \pm 0.03$
N 5297	40.4	$3.00 \pm 0.33$
N 5775	28.9	$7.56 \pm 0.65$
N 5792	31.7	$4.41 \pm 0.37$
N 5907	16.8	$2.21 \pm 0.19$
U 10288	34.1	$0.66 \pm 0.07$

<sup>a</sup> For other galaxy properties, see [3]. <sup>b</sup> From [4]. <sup>c</sup> From [5], unless otherwise indicated. <sup>d</sup> From the mixture method of [6] using the H $\alpha$  flux of [7] and 22  $\mu\text{m}$  flux of [4]. <sup>e</sup> From the IR method of [6] using the 22  $\mu\text{m}$  flux from [4].

Unique to CHANG-ES is the measurement of all polarization products, namely Stokes  $I$ ,  $Q$ ,  $U$ , and  $V$ . With analysis of linear polarization,

$$P = \sqrt{Q^2 + U^2} \quad (\text{when } V = 0) \quad (1)$$

along with rotation measures (RMs), an in-depth understanding of the magnetic fields in these galaxies can be obtained (Section 3.4), and several examples have been very illuminating in this regard. Even circular polarization was observed in some cases (Section 3.1). The polarization results have been some of the most important outcomes of CHANG-ES and can also lead to some stunning images (e.g., Figure 1).

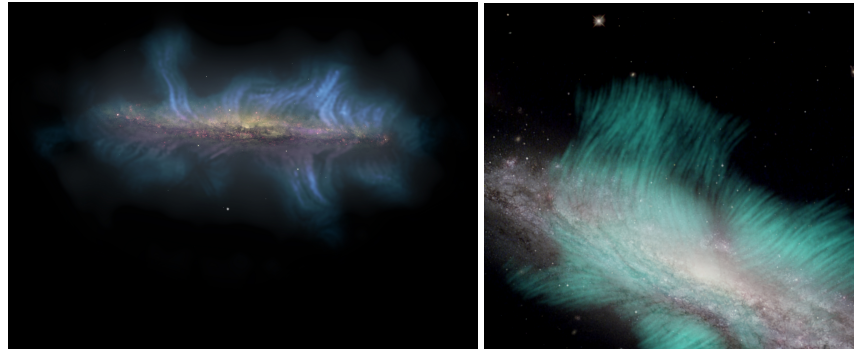


**Figure 1.** See <https://public.nrao.edu/news/2020-image-contest-winners> accessed on 4 May 2024 and [8] for these images which won Second Prize (left) and Honorable Mention (right) in the NRAO image contest held as part of celebrating the 40th anniversary of the VLA. On the left, the magnetic field of NGC 5775 is highlighted in superb detail using the CHANG-ES D-array and C-band linear polarization data. Displayed in fuchsia near the disk and in blue farther out, the curvy field lines are highlighted via an LIC algorithm (Section 2.2.3) and extend as high as 8 kpc from the plane. Superimposed is an optical image constructed from the Hubble Space Telescope data of the galaxy, showing hot ionized gas in rose and broad-band optical in pale yellow. On the right, the magnetic field of NGC 4666 is illustrated using the same LIC algorithm as on the left. Image by Y. Stein with support from J. English. See also [9]. See Figure 8 for versions with coordinates.

CHANG-ES goals include understanding the incidence of radio halos, determining their scale heights, and correlating these results with other properties such as the SFR. A consistent galaxy sample, with complementary data at other wavelengths, can also help us explore pressure balance in the ISM. Measurements of outflow speeds can help to determine whether galaxies are more likely to experience winds or returning ‘fountain flow’. Spatially resolved spectral index maps are essential to this process because they are required when modeling the way in which cosmic ray electrons (CREs) propagate (Section 3.3). On broader scales, details of outflows from CHANG-ES galaxies can be connected to the Circumgalactic Medium (CGM) and to the process of magnetizing the intergalactic medium (IGM). Outflows in nearby galaxies could also be low-energy analogues of the ‘feedback’ that appears to be required in galaxy formation scenarios in order to control the star formation rate [10]. For more information on our original science goals, see [11].

This paper is organized as follows. In Section 2, we describe the technical incentive and details for CHANG-ES, as well as technical advances and data products. In Section 3 we list some research highlights, and in Section 4 we indicate what current research is ongoing and planned. Section 5 provides a summary with open questions.

## 2. Technical Aspects of the Survey and New Advances in Techniques

### 2.1. Technical Overview

CHANG-ES was initially conceived because of the newly available wide bandwidths,  $\Delta \nu$ , afforded by the VLA’s Wideband Interferometric Digital ARchitecture (WIDAR) correlator<sup>2</sup>. A visual representation of the original frequency coverage can be seen in red

and blue in Figure 2 (green refers to subsequent S-band observations, see Section 4). The wide frequency coverage, 500 MHz at L-band and 2 GHz at C-band, has a number of advantages over previous observations. For example, the theoretical signal-to-noise (S/N) ratio increases as  $1/\sqrt{\Delta\nu}$ . For CHANG-ES, this has meant an improvement by an order of magnitude, on average, compared to any previous similar surveys. In addition, these wide bandwidths are broken up into many individual channels. This allows radio frequency interference (RFI) to be more readily identified and excised. It also means that the spatially resolved spectral index can be more readily probed; for example, *in-band* spectral index maps can be formed, e.g., [4]. Images can also be made using multi-scale, multi-frequency synthesis [12,13]<sup>3</sup>, and rotation measure (RM) synthesis, e.g., refs. [14,15] can be used to correct for *Faraday Rotation* (FR, Section 3.4), point-by-point, when multiple spectral channels are available.

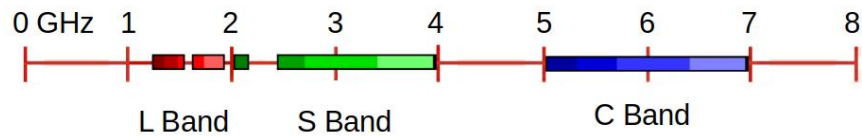


**Figure 2.** Visual representation of the CHANG-ES frequency coverage. The red and blue bands represent the L-band and C-band coverage of the original observations (see [1] for a tabular version), while green represents newer S-band data discussed in Section 4.1. The gaps in L-band and S-band are because of RFI. The gap from 4 to 5 GHz is because the lowest available C-band frequency was 5 GHz during CHANG-ES observations. Shading is for aesthetics and does not indicate any technical differences in the band.

Since in-disk and high latitude features in galaxies show structures on virtually all spatial scales, we required observations over a range of VLA array configurations. Thus we have observed at B-, C-, and D-configurations in L-band and in C- and D-configurations in C-band (see Section 4 for S-band). We use the nomenclature, for example, “D-array L-band”, to specify the VLA configuration and frequency band, respectively. To complement the VLA data, we have also acquired Green Bank Telescope (GBT) single-dish data to fill in missing large scale flux. Analysis of these data is ongoing.

## 2.2. Improved Techniques

In the process of image-making and dealing with wide bands, a number of techniques required careful analysis and, in some cases, improvement over previous studies. In this section, we itemize some of them.

### 2.2.1. In-Band Spectral Indices

Typically, the spectral index,  $\alpha$ , where the spectrum is described as  $I_\nu \propto \nu^\alpha$ , has usually been measured between two separate frequency bands. For example, the specific intensity,  $I_\nu$ , can be measured for the centers of L-band and C-band, and a single value of  $\alpha$  can be measured for each position in the galaxy, as was done for some high-resolution data sets in CHANG-ES (Section 2.3). However, the wide bands (Figure 2) also allow for the formation of *in-band* spectral indices. Two advantages can immediately be identified.

The first is that a single wide-band observation, rather than two separate observations, leads to a map of  $\alpha$  and its error map,  $\Delta\alpha$ . Extensive testing can be found in [4], revealing that, for the S/N of most CHANG-ES galaxies, the calculated in-band  $\Delta\alpha$  values typically underestimate the true uncertainties by  $\approx 20\%$ . This underestimate increases substantially once the distance from the pointing center reaches a point where the primary beam drops to 70% of its peak value.

For brighter and/or smaller angular size sources (or regions of a source), in-band spectral indices are useful tools and, in cases of variability, are essential. A good example is the galaxy NGC 4845, which harbors an AGN. Measurements of the fluxes, in-band spectral



indices, and their variation with time allowed for the modeling of a jet-like outflow in this tidal-disruption-event (TDE) galaxy [16].

In principle, one can also solve for curvature in the spectral index, should it exist. CASA allows for a solution described by  $I_\nu \propto \nu^{\alpha+\beta \log \nu}$ , where  $\beta$  is a curvature term. An early example of a map of  $\beta$  and its error map,  $\Delta\beta$ , can be found in [17]. In general, however, this and other trials have shown that higher S/N is required to generate maps of  $\beta$  with confidence.

### 2.2.2. Thermal/Nonthermal Separation in Edge-on Disks

The nonthermal component of the emission (i.e., synchrotron radiation) dominates over the thermal component (i.e., thermal Bremsstrahlung radiation) globally in spiral galaxies, as is clearly evidenced by strongly negative spectral indices, e.g., refs. [4,18,19], and others. However, a thermal component contributes importantly to the total emission and must be corrected for, if the nonthermal emission and nonthermal spectral index are to be measured and understood. A standard method is to use H $\alpha$  and/or IR maps to provide the needed thermal information. The thermal map can then be subtracted from the total emission radio map to obtain the nonthermal emission and spectral index maps.

Because previous H $\alpha$ -to-thermal calibrations, e.g., refs. [20,21] did not focus specifically on edge-on systems, however, the question arises as to how well these calibrations work for long lines of sight in which dust obscuration is significant. Early evidence from [3], for example, suggests that dust absorption could be underestimated in CHANG-ES galaxies.

Therefore, H $\alpha$  imaging was obtained for CHANG-ES galaxies to provide information on star formation and ionized gas morphologies, and to carry out tests of the thermal/nonthermal separation [5,6]. A method was developed to estimate the thermal radio emission using H $\alpha$  data combined with Wide-Field Infrared Survey Explorer (WISE) IR data to enable this separation. We showed that a combination of both of these data provides a better estimate of star formation rates, hence of the ionized gas thermal emission, than using either tracer alone. The edge-on perspective of the galaxies led to a slightly modified “mixture method” formula than the one empirically determined in [21]. The modification involves a 35% higher weight to the WISE band 4 data. We derived nonthermal radio maps for three galaxies using this method [6], and demonstrated that the nonthermal spectral index in these galaxies shows a systematic steepening with vertical height above the plane, as might be expected from cosmic ray aging due to synchrotron electron energy loss. The mixture method is currently being applied to the entire sample for a more global study.

### 2.2.3. New Techniques in Image Display

In Figure 1, we show the plane-of-sky magnetic field lines in NGC 5775 (left) and NGC 4666 (right). This ‘flow-line’ technique using a Line Integral Convolution (LIC) algorithm, ref. [22] (adapted by A. Miskolczi, Y. Stein, and J. English) is becoming more common when displaying magnetic field lines, as opposed to the more conventional ‘dashes’, such as shown in Figure 6. It allows the nature of the fields to be enhanced where the polarization is stronger and is easily adaptable to additional color enhancements in different regions, as was done in Figure 1.

We have also developed perceptually based color maps for spectral index images and error maps [23] specifically for the CHANG-ES catalog panels, as shown in [4] and on the public data release website (described in Section 2.3). In Figure 3, we show the B-array L-band to C-array C-band spectral index map of NGC 3079. A description of how this map and its corresponding error map were generated can be found in [24]. The spectral index color table has two main divergent points and the default settings for the values of these points are based on physics and adopted definitions for “steep” slopes ( $\alpha$  more negative than  $-0.8$ ) and “flat” slopes ( $\alpha$  more positive than  $-0.1$ ) in the radio regime. This makes the map immediately useful. Values for these points can also be changed by the user. A third divergent point (gray-ish) lays between these threshold values. Two pairs of perceptually complementary colors are employed and, incorporating a redundancy cue,

the map is monotonic in grayscale values with the lightest colors for steep slopes and darkest colors for flat slopes. The corresponding two-color error map is represented by a single point divergent scheme that is not in visual conflict with the spectral index map. Both  $\alpha$  and  $\Delta\alpha$  maps, as visually rendered for NGC 3079, can be seen on the public data release website<sup>4</sup>. The yellow and gray  $\Delta\alpha$  map on this site shows that the error in the  $\alpha$  map in Figure 3 is less than 0.1 within the galaxy, except for the blue-purple rim outlining the emission and for purple circles near each end of the major axis. Python Jupyter Notebook [25] tutorials, provided on a GitHub site [26] called CosmosCanvas, describe how to employ the Python code and demonstrate how the schemes can be adjusted (see <https://github.com/mlarichardson/CosmosCanvas> (accessed on 4 May 2024)).

The complementary colors not only help retain the viewer's attention, but also permit almost “at-a-glance” discoveries. This is shown in Figure 3, where the dark plum color pinpoints the flat spectral index associated with an AGN in the center of NGC 3079.

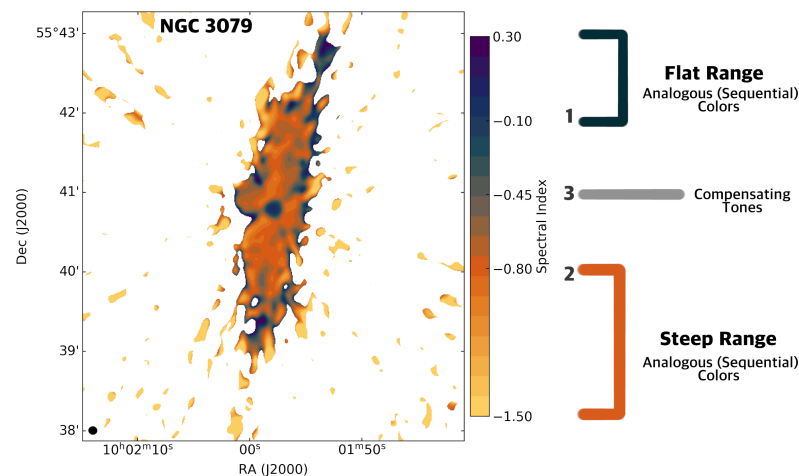


**Figure 3.** Spectral index color map: this triple divergent color scheme has 3 boundaries. Boundary 1 is assigned cyan and the increasingly positive values of  $\alpha$  have sequential colors on a standard color wheel. Cyan's complementary color, orange, marks divergent point 2, the upper boundary for “steep” spectral values, and colors of more negative  $\alpha$  are also sequential. The end points of the color bar are yellow and purple which are also complementary colors, which work with human color perception. The gray-ish divergent point 3 is created by mixing the orange and cyan in steps to create tones of intermediate color. This example demonstrates that a flat spectrum central AGN can be discerned almost at a glance with this color scheme. Tutorials for this, along with a single divergent point error map, are found at <https://github.com/mlarichardson/CosmosCanvas> (accessed on 4 May 2024).

### 2.3. Public Data Release Website

The CHANG-ES public website is <https://projects.canfar.net/changes>. It should be noted that this website has superseded the previous public release website that was announced in [1] and in earlier papers<sup>5</sup> Table 2 lists all of the data products that are available to date. These data are in Flexible Image Transport System (FITS) format and are freely available for download.

**Table 2.** Available FITS images at <https://projects.canfar.net/changes> (accessed on 4 May 2024).

Type of Observation	No. of Galaxies	Ref
Radio Images		
D-array L-band		
Total Intensity <sup>a,b</sup>	35	[4]
Linearly Polarized Intensity <sup>a,b</sup>	35	[4]
Polarization Angle <sup>a</sup>	35	[4]
In-band spectral Index <sup>c</sup>	35	[4]
Spectral Index Error maps <sup>c</sup>	35	[4]
D-array C-band		
Total Intensity <sup>a,b</sup>	35	[4]
Linearly Polarized Intensity <sup>a,b</sup>	35	[4]
Polarization Angle <sup>a</sup>	35	[4]
In-band spectral Index <sup>c</sup>	35	[4]
Spectral Index Error maps <sup>c</sup>	35	[4]
C-array L-band		
Total Intensity <sup>a,b</sup>	35	[27]
Linearly Polarized Intensity <sup>a,b</sup>	35	[27]
Polarization Angle <sup>a</sup>	35	[27]
C-array C-band		
Total Intensity <sup>a,b</sup>	35	[27]
Linearly Polarized Intensity <sup>a,b</sup>	35	[27]
Polarization Angle <sup>a</sup>	35	[27]
B/L to C/C spectral Index <sup>d</sup>	35	[28]
Spectral Index Error maps <sup>c</sup>	35	[27]
B-array L-band		
Total Intensity <sup>a,b</sup>	35	[24]
Linearly Polarized Intensity <sup>a,b</sup>	35	[24]
Polarization Angle <sup>a</sup>	35	[24]
B/L to C/C spectral Index <sup>d</sup>	35	[28]
Spectral Index Error maps <sup>c</sup>	35	[24]
L-band (all arrays, RM corrected)	21	[29]
C-band (all arrays, RM corrected)	21	[29]
H $\alpha$ Images	27 <sup>e</sup>	[5]
H I Images	19	[30]

<sup>a</sup> In most cases, two spatial resolutions are available, made with two different uv weightings. <sup>b</sup> Maps, both corrected and uncorrected for the primary beam, are available. <sup>c</sup> Corrected for the primary beam. <sup>d</sup> B/L = B-array L-band, C/C = C-array C-band. The same maps are accessible from the B/L or C/C area. <sup>e</sup> Twenty-four galaxies were observed with the Apache Point Observatory (APO) and three are taken from available literature.

It should be noted that, at high resolution, where emission is weaker, we opted to include band-to-band spectral index maps, rather than in-band spectral index maps, i.e., B-array L-band to C-array C-band  $\alpha$  maps with their error maps. Future D-array C-band to C-array L-band  $\alpha$  maps are forthcoming. The H $\alpha$  images were obtained to assist with the thermal/nonthermal separation analysis (Section 2.2.2). Remarkably, H I ‘MOM0’ images were also successfully extracted from CHANG-ES data, some images for the first time see [30]—another (unexpected) consequence of having narrow channels across L-band.

The public release website also lists CHANG-ES publications as well as some press releases. In addition, but not on the website, we have other ancillary data, such as WISE-enhanced resolution images of all galaxies, to assist with the thermal/nonthermal separation (Section 2.2.2), as well as XMM-Newton and Chandra data [31] for a large fraction of the sample. More CHANG-ES companion data will be described in Section 4.

### 3. CHANG-ES Science Highlights

#### 3.1. Into the Core—Active Galactic Nuclei

Determining whether the core of a spiral galaxy is dominated by a star formation or by an AGN has historically been a challenge. Although all galaxies are expected to harbor a supermassive black hole (SMBH), e.g., ref. [32], this does not necessarily imply strong AGN activity. Such activity could be absent, for example, if there is little accretion onto the SMBH. It could also be absent in a lull period if the activity is episodic, e.g., ref. [33]. Weak AGNs, called low-luminosity AGNs (LLAGNs) [34,35], might also be present but simply masked by other types of emission.

For edge-on galaxies, where the line of sight is large at the center, radio frequencies have a clear view down to the core. High angular resolution is also required to help disentangle the core region from the surrounding local disk. CHANG-ES B-array L-band (B/L) and C-array C-band (C/C) provide  $\approx 3$  arcsec resolution, corresponding to linear resolutions from approximately 64 to 610 pc. In [24], we adopted a number of criteria to help determine whether or not an AGN is present in a galaxy. The radio criteria are as follows: (1) the presence of point-like cores, (2) a luminosity that is too high for a collection of SNe, (3) flat or positive spectral indices at the center, (4) the presence of bipolar or lobe-like structures, (5) time variability, and (6) circular polarization (CP). For nineteen galaxies, X-ray emissions were also interrogated and eight of these showed evidence for AGNs from their X-ray spectra. In some cases, a single criterion may not be sufficient; for example, bipolar structures (criterion # 4) can also result from starburst winds. However, bipolar structure visible in polarization, but not at total intensity, is an AGN signature. Similarly, a circularly polarized core, which has been detected in some CHANG-ES galaxies [16,36], also rules out a thermal origin.

Figure 4 illustrates two examples of CHANG-ES galaxies that reveal previously undetected bipolar radio structures, suggestive of AGNs. The left (NGC 5792) galaxy shows radio lobes centered on the galaxy nucleus. These lobes are seen in linear polarization but are masked in the total intensity images, clearly ruling out a starbursting (thermal) origin. The right figure (NGC 3628) similarly shows a bipolar emission centered on the nucleus but this time via the total intensity spectral index map. It has long been known that maps of spectral index show more structure than total intensity images, e.g., Figure 2 from [37], and this is the case for NGC 3628; together with the criteria outlined in the previous paragraph, this galaxy also likely has an AGN. Another striking example (not shown) is NGC 2992, described in [38].

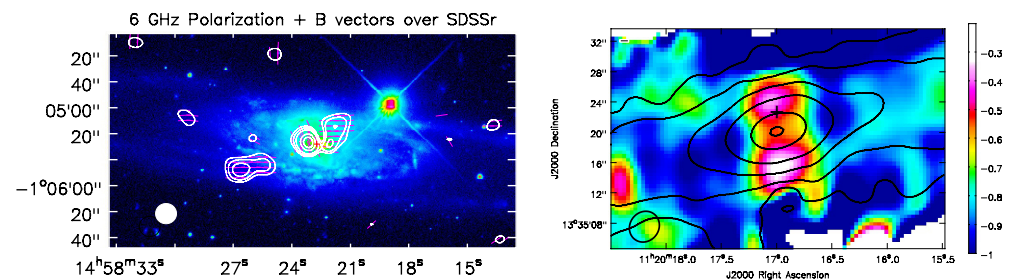


**Figure 4.** On the left, polarization contours plus B-field orientations over a grayscale optical SDSS image of NGC 5792, from [39]. On the right, L-band total intensity contours over the B/L to C/C spectral index map of NGC 3628 [24].

We were able to use the criteria specified above to probe 33 CHANG-ES galaxies, finding evidence for an AGN in 18 galaxies [24]. Since that paper was published, the galaxy NGC 5792 was also shown to have bipolar polarized radio lobes [31,39] (Figure 4 left), and the galaxies NGC 4192 and NGC 3877 are also new LLAGN candidates [31]. NGC 3877 also appears to be time variable. Altogether, then, we have uncovered evidence for AGN activity in 64% of 33 CHANG-ES galaxies. This high proportion is due to the fact that radio frequency observations can peer down into the core of systems that are edge-on; the high sensitivity of CHANG-ES data allows us to detect faint LLAGNs, especially the polarization data, that uncover AGN-related activity. As noted in Section 1, the sample selection did not include any AGN-related criteria, so it is likely that a random sample of face-on galaxies would show similar proportions if similar criteria are used.

### 3.2. Discrete Sources in and Around the Disks

The high-resolution data, described in Section 3.1 have also been used to search for other radio sources besides AGNs. In [31], we present catalogs of discrete radio and X-ray sources using data from both CHANG-ES frequencies as well as the Chandra satellite. The three new

candidates for LLAGNs identified in Section 3.1 were detected in this study, based on their radio and X-ray properties. In addition, we found new nuclear sources in two companion galaxies: NGC 4298 (companion to the CHANG-ES galaxy, NGC 4302) and NGC 4435 (companion to NGC 4438). Two examples of other new discoveries are shown in Figure 5. On the left is the galaxy NGC 4438, showing two sources (fuchsia dots). The central source is the AGN, but the source approximately 2 arcmin to the south is an X-ray source with a previously unknown corresponding radio source. On the right is a binary star system in the Milky Way, observed near NGC 4594 (the Sombrero Galaxy). This unexpected discovery shows radio and X-ray emissions that likely signify some interaction between the two active stars.

These catalogs provide a base for follow-up studies to confirm the nature of the discrete sources, investigate their origin and evolution, and understand their potential impact on the ecosystems of the edge-on galaxies.



**Figure 5.** Sample images from [31]. On the left, an optical image of NGC 4438 is shown in colour. Two compact sources are specified in fuchsia. The central source is the AGN, and the southern source is a new cross-matched radio/X-ray source. On the right, an optical Milky Way binary star system is shown in colour. These stars are near the Sombrero galaxy and have Gaia designations 530134264552397440 (right star) and 3530134264552424960. The blue and red dots and error ellipses show the positions of the L-band and C-band sources, respectively. The black dots with error circles denote the two X-ray sources. The scale showing 1 arcsec is displayed on the lower left.

### 3.3. Cosmic Ray Propagation—Outflows and Winds

One of the main science goals of CHANG-ES is to investigate the nature of radio halos. They indicate the presence of cosmic-ray electrons and magnetic fields, which are nowadays thought of as playing crucial roles in the development of galactic winds. This subject was recently reviewed in [40], but, here, we provide a brief summary of aspects that are particularly relevant to CHANG-ES. Cosmic ray transport can be described as diffusion and advection, the latter being important in the case of galactic winds. Hence, a study of the cosmic-ray electron transport may allow us to detect galaxies with winds and explore the role of cosmic rays in them. An early study of the edge-on galaxy NGC [41], using the Westerbork Synthesis Radio Telescope (WSRT) compared diffusion and advection models with the  $z$ -distribution of intensity and the radio spectral index at GHz frequencies. A more recent multi-wavelength study of the Milky Way [42] gives a global context including cosmic rays, gamma rays, calorimetry (Section 3.3.2), and a spectrum of our galaxy as it would be seen from one of our CHANG-ES galaxies.

CHANG-ES galaxies have been analyzed with SPINNAKER (SPectral INDEX Numerical Analysis of K(c)osmic-ray Electron Radio-emission; ref. [43]), which models radio continuum data based on models of pure diffusion and advection. It should be noted that both diffusion and advection may (or may not) be escape-dominated, either with CR electrons diffusing or ‘blowing’, respectively, into the ICM.



### 3.3.1. Advective and Diffusive Halos

The scale height analysis of [44] shows that radio halos in CHANG-ES galaxies are escape-dominated. This can be shown in an indirect way using two arguments. First, the galaxies have exponential vertical radio intensity profiles. This is something that we would expect for cosmic-ray electron advection rather than diffusion from theoretical grounds [43]; there are also observations that corroborate this view by observing examples of Gaussian halos that would be in favor of diffusive halos [9,19,43,45]. This underlines that, in CHANG-ES galaxies, cosmic-ray advection rather than diffusion plays the dominant role. Second, the ratio of scale heights at low and high frequencies indicates that loss processes are not important as the ratio falls in between what is expected for escape-dominated halos and either advection or diffusion. Furthermore, we find that diffusion has a mild energy dependency in both face-on [46] and edge-on galaxies [47]. Also, scale heights are larger in larger (more massive) galaxies [44]. This could be a geometric effect, where the opening of the magnetic field lines is regulated by the galaxy size, as found, for instance, in models of galactic winds. However, when a normalized scale height is computed, which accounts for the size of the galaxy, we see an anti-correlation, such that larger, more massive galaxies have smaller normalized scale heights. This suggests that the massive galaxies are more effective at retaining CR electrons.

Similar results are found when studying the spatially resolved intensity profiles. This has the advantage that the shape of the intensity and radio spectral index profiles can be taken into account without the simplification of assuming either exponential or Gaussian intensity profiles. Out of the 35 CHANG-ES galaxies, 11 were analyzed in this way. In addition, eight galaxies were analyzed, which are either not in the CHANG-ES sample or only have VLA legacy data available for the analysis. In Table 3, we summarize the findings of Heesen [40], updated with new publications that have appeared since. Of the eleven CHANG-ES galaxies, two have diffusion-dominated halos (NGC 4013 and NGC 4565) with the remainder advection dominated. Of the nineteen galaxies studied in total, three are diffusion-dominated. Hence, advection-dominated radio halos are the norm rather than the exception. Moreover, winds accelerate with  $z$ -height, e.g., refs. [18,47,48]. In one case, that of NGC 5775, we have a mass loss rate estimate of  $\dot{M} = 3 \rightarrow 6 M_{\odot}/\text{yr}$  [49]. The best-known discriminator thus far is the star-formation rate surface density (SFRD). Galaxies at low SFRDs have diffusive halos. By contrast, at high SFRDs, they have advective halos [40]. It should be noted that this does not imply that the scale heights are higher for more intensely star-forming galaxies; rather, the sizes of advective halos are regulated by galaxy size instead [44].

**Table 3.** CR electron transport properties of edge-on galaxies. The displayed results are derived by fitting two vertical intensity profiles at two radio continuum frequencies with the 1D transport code SPINNAKER. CHANG-ES galaxies are highlighted in bold.

Galaxy	Distance [Mpc]	Freq. [GHz]	Model <sup>a</sup>	$D_0$ [cm <sup>2</sup> s <sup>−1</sup> ] × 10 <sup>28</sup>	Velocity [kms <sup>−1</sup> ]	Ref
IC 10	0.8	[0.144, 1.6]	Adv.	-	29 ± 8	[50]
NGC 55	1.9	[1.4, 4.8]	Adv.	-	100 ± 50	[51]
NGC 253	3.9	[1.4, 4.8]	Adv.	-	400 ± 100	[51]
<b>NGC 891</b>	9.1	[1.5, 6]	Adv.	-	150 ± 50	[18]
		[0.144, 1.5]	Adv. flux tube	-	410 ± 70 <sup>b</sup>	[47]
<b>NGC 3044</b>	4.4	[1.4, 4.8]	Adv.	-	200 ± 130	[51]
<b>NGC 3079</b>	7.7	[1.4, 4.8]	Adv.	-	350 ± 70	[51]
<b>NGC 3556</b>	14.09	[0.144, 1.5]	Adv. with acc.	-	340	[48]
<b>NGC 3628</b>	14.8	[1.4, 4.8]	Adv.	-	250 ± 150	[51]
<b>NGC 4013</b>	16.0	[0.15, 1.5, 6]	Diff. ( $\mu = 0$ )	0.6 ± 0.05	-	[52]
		[0.144, 1.5]	Diff. ( $\mu = 0$ )	1.4 <sup>+2.8</sup> <sub>−0.7</sub>	-	[47]
<b>NGC 4157</b>	15.6	[0.144, 1.5]	Adv. flux tube	-	450 ± 50 <sup>b</sup>	[47]
<b>NGC 4217</b>	20.6	[1.5, 6]	Adv.	-	350 ± 100	[19]
<b>NGC 4565</b>	11.9	[0.144, 1.6]	Diff. ( $0 \leq \mu \leq 0.5$ )	2.0 ± 0.9	-	[51]
		[1.5, 6]	Diff. ( $0 \leq \mu \leq 0.3$ )	≥ 2.0	-	[18]
<b>NGC 4631</b>	6.9	[1.4, 4.8]	Adv.	-	250 ± 60	[51]
	7.4	[0.144, 1.5]	Adv. flux tube	-	320 ± 70 <sup>b</sup>	[47]
<b>NGC 4666</b>	26.6	[1.5, 6]	Adv.	-	310 ± 50	[9]
<b>NGC 5775</b>	26.9	[1.4, 4.8]	Adv.	-	400 ± 80	[51]
		[0.140, 1.5]	Adv. flux tube	-	600 ± 200 <sup>b</sup>	[49]
<b>NGC 7090</b>	10.6	[1.4, 4.8]	Adv.	-	200 ± 160	[51]
<b>NGC 7462</b>	13.6	[1.4, 4.8]	Diff. ( $\mu = 0.5$ )	2.4 ± 0.4	-	[51]

<sup>a</sup> Models are for pure advection (Adv.) and diffusion (Diff.) with the diffusion coefficient  $D = D_0(E/\text{GeV})^\mu$ ; advection models have constant speeds (Adv.), linearly accelerating speeds (Adv. with acc.), and accelerating speeds described by an isothermal galactic wind in a flux tube (Adv. flux tube). <sup>b</sup> For the accelerated wind models, we quote the maximum derived velocity.

### 3.3.2. Calorimetry of Galaxy Disks and Halos

The concept of galaxies as ‘calorimeters’ was introduced by [53] to help explain the well-known far infrared (FIR)–radio correlation, an almost linear relation between the radio and FIR in galaxies over many orders of magnitude. If both FIR emissions and abundance of CR electrons are proportional to the supernova rate, this would explain the correlation, assuming that the effects of varying magnetic fields are minor. FIR emissions result from the heating of dust in star-forming (SF) regions and CRs are produced by supernovae, in SF regions as well. This requires that both dust and CR electrons are ‘trapped’ together, hence the concept of the calorimeter. There is a rich history of literature that attempts to explain this relation, adjusting it for differing frequency bands, testing for non-linearity, including correlations with the magnetic field [54], or ensuring that all necessary emissions are taken into account, such as  $\gamma$ -ray emissions. The Milky Way, for example, appears to be a good calorimeter when all CR-related luminosity tracers are included [42].

However, if CR electrons are *not* trapped, but escape, as we generally find in CHANG-ES galaxies (Section 3.3), then the galaxy is no longer a calorimeter. A plot of radio luminosity against FIR luminosity (or star formation rate, SFR) should produce a slope that is sublinear, since CR electrons can escape but dust is generally confined to the disk. On the other hand, if the magnetic field increases with SFR, as suggested by the non-calorimetric model of [54], then so should the radio luminosity, and superlinear slopes should result. In either case, non-linear slopes are expected when there are departures from the calorimetric condition.

Because the CHANG-ES sample is of edge-on galaxies, the calorimetry efficiency can be investigated for the disk and halo as a whole. In [3], we found tight correlations between the radio luminosity and SFR (as measured from the mid-IR), consistent with previous authors<sup>6</sup>. In C-band, we find a slope that is consistent with a calorimeter ( $L_{6\text{ GHz}} \propto \text{SFR}^{1.057 \pm 0.075}$ ) but in L-band, where the lifetime of CR electrons is larger, we find modest departures from calorimetry as a *superlinear* slope ( $L_{1.6\text{ GHz}} \propto \text{SFR}^{1.132 \pm 0.067}$ ). Therefore, some important additional effects, such as increasing magnetic fields with increasing SFRs as suggested above, or a higher fraction of SN energy transported into CRs with higher SFRs, may be at play. See [3] for further discussion of other subtleties such as cooling timescales, and discussions of escape-dominated, or loss-dominated regimes.

### 3.4. Magnetic Fields and Their Orientation

The CHANG-ES galaxy sample shows a variety of magnetic field patterns, as we outline in this section. However, when the 6 GHz images are ‘stacked’, an underlying dominant pattern emerges. To accomplish this, Stokes Q images of 28 galaxies were combined, as were Stokes U images. Each image was rotated so that the major axis was in the horizontal direction, scaled to the size of the largest galaxy, flux-corrected for distance, and weighted by the S/N, point-by-point. The resulting stacked Q and U images were then combined, as in Equation (1), to make the polarized image shown in Figure 6, left (see also [29] for more details). The emergent pattern is that of an overall (ragged) ‘X-shaped’ magnetic field. This is not the first time that X-shaped fields have been observed, e.g., ref. [55], but it is the first time that this geometry has been shown to be a common feature of galaxies. Had the fields been purely random, or only associated with galaxy-specific SF regions, no such pattern would have emerged in a stacked sample. The observed magnetic field should be a mixture of plane-parallel disk fields, and halo fields with a dominating vertical component. An observed X-type field suggests either that both fields have similar strengths in similar regions, or that this pattern is an intrinsic property of galaxies (see, e.g., Section 3.6). The pattern also indicates that the CHANG-ES galaxies have ‘scalable’ large-scale fields, since the 28 galaxies, which spanned a factor of 9 in angular size, were brought to a common size prior to stacking.

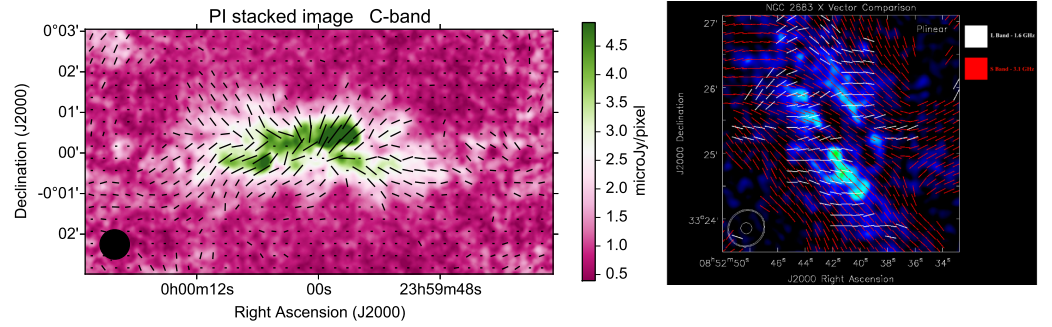


**Figure 6.** On the left, the weighted mean linear polarization (colors) and matching magnetic field orientations from the stacking of 28 CHANG-ES galaxies, showing an underlying X-shaped field, from [29]. The RA and Decl. axes have arbitrary centering. On the right, Comparison between C-band (red) and L-band (white) magnetic field (B) orientations at the same resolution in the galaxy NGC 2683, superimposed on an S-band (Section 4) polarization image. The galaxy’s major axis extends from the north-east to the south-west. It should be noted how much the B field orientation has rotated between C-band and L-band. From [56].

It is important to note that polarized emission is a signature of *ordered* fields (isotropic turbulent fields, for example, do not produce polarization). Ordered fields may have contributions from large-scale *regular* fields, generated by dynamo action, and *anisotropic turbulent fields*, generated by compression or shear of isotropic turbulent fields [57]. Figure 1 of [58] provides a useful illustration. Regular fields give rise to significant Faraday rotation (FR, described below), while anisotropic random fields reveal negligible FR when integrated over the line of sight. In nearly face-on galaxies, the anisotropic turbulent fields are several times stronger than regular fields [58].

The strength of ordered fields that give rise to polarization can be obtained from the strength of the total field (obtained from the total synchrotron emissions and an assumption of equipartition) along with the fraction of synchrotron radiation that is polarized,  $P$ . It should be noted that a polarized emission measures the component of the magnetic field that is in the plane of the sky,  $B_{\perp}$ . To obtain the strength of the regular field along a line of sight, we require Faraday rotation analysis.

The angle that a polarized wave rotates as it passes through an ionized medium is

$$\Delta\Phi = FD\lambda^2 \quad (2)$$

where

$$FD = k \int n_e B_{\parallel} dl \quad (3)$$

is the *Faraday depth* (sometimes just called the rotation measure, or RM)<sup>7</sup>,  $k$  is a constant,  $n_e$  is the thermal electron density,  $B_{\parallel}$  is the strength of the magnetic field parallel to the line of sight, and  $l$  is the line of sight distance through the medium. By convention,  $FD$  is positive when the field points towards the observer, and negative if the field points away. Clearly, if the line of sight is very large, the rotation will be greater for polarized emissions coming from the back of the cloud in comparison to the front. This differential FR means that the emerging light has contributions from many angles and is, therefore, depolarized, even if the internal field is regular. In general, depolarization of the disk is likely a combination of accumulation of small-scale structure along the line of sight and within the beam (wavelength-independent depolarization), Faraday dispersion due to turbulent fields, and differential Faraday rotation along the line of sight within the beam and across the observed frequency band (wavelength-dependent depolarization). This places an effective ‘depth’ on the emission such that, if  $\lambda^2 \Delta\Phi \gg 1$ , the source is ‘Faraday thick’. We can only recover information about  $B_{\parallel}$  if the source is Faraday thin.

There are two important consequences that are relevant to CHANG-ES. The first is that observations at L-band (longer  $\lambda$ ) can be strongly depolarized, showing little to no polarization. The second is that, if L-band polarization *is* observed, it can suffer from significant Faraday rotation compared to C-band. Figure 6 (right) shows a striking example in NGC 2683. Here, we see C-band magnetic field (B) orientations in red and L-band orientations in white, from matching resolution data. In L-band, the galaxy has been almost completely depolarized along the major axis where the line of sight is large, and the polarized emission does not extend out very far from the major axis, in comparison to C-band. In addition, the B orientations in L-band have been significantly Faraday-rotated compared to C-band.

For these reasons, we have carried out rotation measure analysis using C-band data. To obtain images of Faraday rotation measures (RMs), we applied RM-synthesis [14] to the CHANG-ES data [29]. RM-synthesis provides images of polarized intensity that are not affected by differential Faraday rotations within the observed frequency range, and, also, an image of rotation measures up to a maximum rotation measure set by the differential Faraday rotation within a single frequency channel. This has allowed us to analyze the halo fields as well as the disk fields of the galaxies in unprecedented detail.

#### 3.4.1. Large-Scale Ordered Magnetic Fields in CHANG-ES Galaxies

Of all thirty-five CHANG-ES galaxies, all except one<sup>8</sup> showed polarized emission at C-band [29]. Seven galaxies showed polarization but were too weak to carry out RM synthesis analyses. Six more were dominated by a central AGN-like source or a background radio galaxy (UGC 10288) and did not have a clear polarized disk or halo emission. This left 21 galaxies for which RM-synthesis was successfully carried out to reveal extended PI within their disks and/or halos and for which reliable RM values could be mapped. An example is shown in Figure 7.

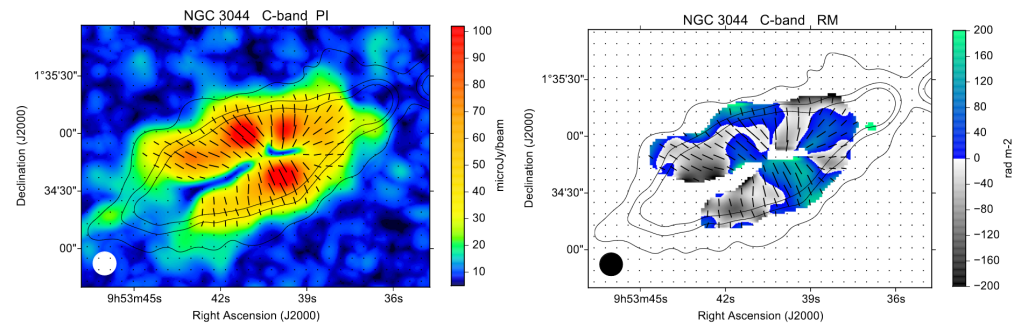


**Figure 7.** NGC 3044 C-band polarized emission, RM-corrected, from [29]. Contours denote the total intensity and show that the major axis extends from the north-west (advancing side) to the south-east (receding side). On the left, the polarized intensity (color) with magnetic field orientations superimposed. On the right, the rotation measure map (color), with magnetic orientations superimposed (see Section 3.4.3).

Five main magnetic field types can be identified from the entire sample:

1. Disk-halo type, where the disk field and the halo field are both observed. This results in classical X-shape type magnetic field structures that can be seen in individual galaxies (NGC 891, NGC 4217, NGC 4631, and NGC 5775). In some cases of close-by galaxies, polarization appears in flocculent patches (NGC 891 and NGC 3556). Due to higher linear resolution, we observe more detail, while the large-scale emission is harder to detect.
2. Disk-type, where the disk field is predominant. These galaxies show little or no polarization originating from the halo, and the observed polarization is mainly parallel to the disk (NGC 3628, NGC 4013, NGC 4192, NGC 4302, NGC 4565 and NGC 5907).
3. Halo-type with a predominant halo magnetic field structure and weak observed parallel disk field. Halo-type magnetic field structures are observed as a dominant



vertical field. The vertical structure is either accompanied by large scale structures (NGC 3044) or, again, by showing flocculent polarization patches with vertical fields (NGC 4631).

4. Large-scale ordered fields that are related to huge outflows from a nuclear region with strong star-formation activity (NGC 3079 and NGC 4388).
5. No large-scale ordered magnetic fields were observed in five of the twenty-one galaxies. In a few galaxies, this is probably a detection bias, where we just did not observe long enough to see the low polarized emission. It would be interesting to investigate if a non-detection could be due to turbulent magnetic fields in the galaxy. This could be analyzed further with deeper observations.

No indication is found in [29] that the existence of a large-scale ordered field is preferentially observed in galaxies with certain Hubble types or with star formation rates. However, we do observe that the degree of polarization,  $P$ , *increases* from the galactic mid-plane to the outer boundary of the halo. This cannot be explained by diminishing thermal emission, given the vertical extent of the decline, and, therefore, suggests increasingly ordered fields with  $z$ -height. Two examples are shown in Figure 8.

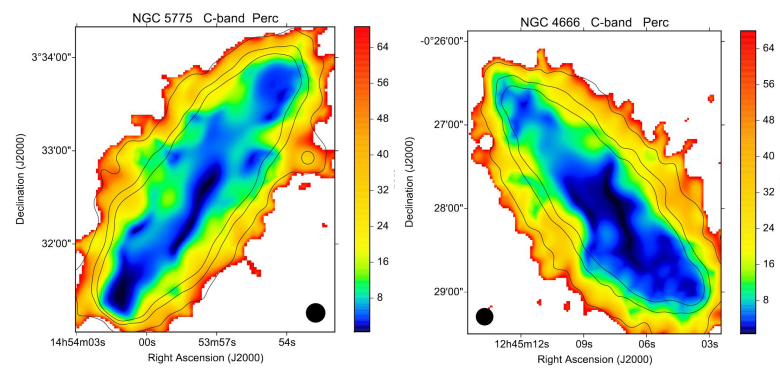


**Figure 8.** Percentage of polarization in NGC 5775 (**left**) and NGC 4666 (**right**) in color. Contours represent the total intensity emission and the beam size is displayed as a filled black circle in a lower corner. From [29]. Attractive images of these galaxies are shown in Figure 1.

### 3.4.2. Asymmetry of Polarized Intensity Between the Advancing/Receding Sides

Most of the CHANG-ES galaxies with observed large-scale polarized emissions at C-band show the strongest polarized intensity (PI) on the side of the major axis that is approaching with respect to the global rotation of the galaxy (13 out of 18, or 72%, [29]). This has been observed in a previous galaxy sample by [60] and was first detected in a CHANG-ES galaxy (NGC 4666) by [9]. An earlier, more sensitive map of NGC 4666 by [61] also shows the asymmetry. We show another example from CHANG-ES, the galaxy NGC 3044, in Figure 7 (left). The absence of polarization in a rough line right along the major axis should also be noted.

The first conclusion [29] is that significant Faraday depolarization is still occurring at C-band, especially along the major axis where the lines of sight are large. The second conclusion is the asymmetry itself, which requires an explanation as to why polarization favors the advancing side for most galaxies. A simplified model is given in [19] (see their Figure 28), where trailing spiral arms may explain the asymmetry in the disk and its correlation with galactic rotation if the polarized emission from the near side of the galaxy dominates because the Faraday depolarization blocks the farther side. However, we also observed this asymmetry, in some cases, in the halo as well, which, in this model, would require both depolarization as well as magnetic spiral arms in the halo. Neither have observational confirmation at present, although halo turbulence, for example, could satisfy the former, and magnetic spirals that ‘lift’ into the halo [62,63] could satisfy the latter. Further work to understand this phenomenon is ongoing, but preliminary results for both L- and C-bands in both C and D arrays appear to be in agreement that the advancing side has stronger polarization.



### 3.4.3. Large-Scale Regular Magnetic Field Patterns in Galaxy Halos

Our images of Faraday rotation measures (RMs) have revealed unprecedented and unexpected patterns of regular fields in halos. Early large-scale dynamo theory (assuming symmetric gas distributions) predicts regular fields of quadrupolar or dipolar shape [64], which, however, are not seen in the CHANG-ES data. More complex patterns are observed instead. Apparently, astrophysical phenomena like spiral arms, galactic winds, and locally strong star formations, can lead to more complex magnetic field patterns. For example, a pattern of dynamo-generated magnetic spiral arms that extend into halos may be adequate (see Section 3.6).

In NGC 4631 a quasi-periodic RM pattern with several sign reversals parallel to the disk on a scale of about 2 kpc was found in the northern halo of the galaxy [65]. These field reversals, together with the observed polarization angles, have been interpreted as giant ‘magnetic ropes’, oriented almost vertical to the galactic plane, but pointing towards or away from the observer, and reaching heights of about 2 kpc (Figure 9). This is the first time that such large-scale regular reversing magnetic field patterns have been seen in any external galaxy. Figure 7 (right) shows another example in which we see positive (color) and negative (grayscale) RMs. Further investigation, moreover, shows that, when RM patterns can be measured in CHANG-ES galaxies, they all reveal some reversals [29].

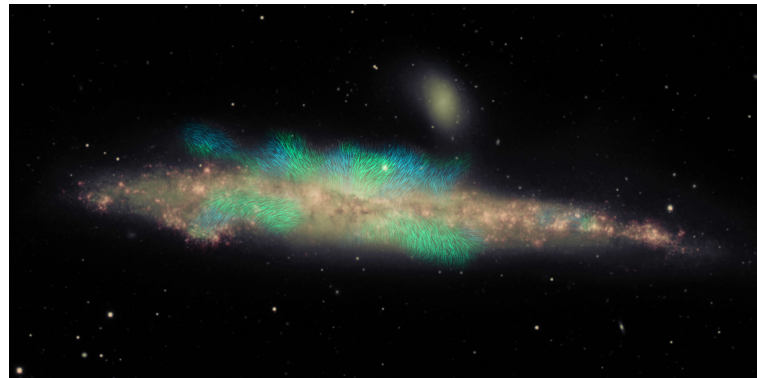


**Figure 9.** Magnetic field orientations of NGC 4631 Faraday rotations measures (from [65]) with RM signs plotted in color (blue: negative, green: positive). Position angles are traced using an LIC algorithm as in Figure 1. The background optical image uses data from the Mayall 4-m telescope, collected by Maria Patterson and Rene Walterbos of New Mexico State University. Image composition by Jayanne English, University of Manitoba.

Other more galaxy-specific halo patterns were also observed. In NGC 4217 (Figure 10, left), a helical outflow structure is present in the northeastern part of the galaxy, extending almost 7 kpc into the halo, as well as bubble-like features on the western side [19]. Large magnetic features were also discovered in the halo of NGC 4388 (Figure 10, right). Two almost vertical filaments with projected extensions of about 4 kpc to the north and 2 kpc to the south are probably related to the outflow from the active nuclear region [66]. The RM data indicate that the fields have a helical shape [67]. Other intriguing features in NGC 4388 are two extended extraplanar blobs of polarized emission at large distances (about 4 kpc) north-west and south-east from the galaxy center. It should be noted how much structure is revealed in polarization that otherwise is not seen at total intensity (where the rms noise is higher), as shown in the inset.

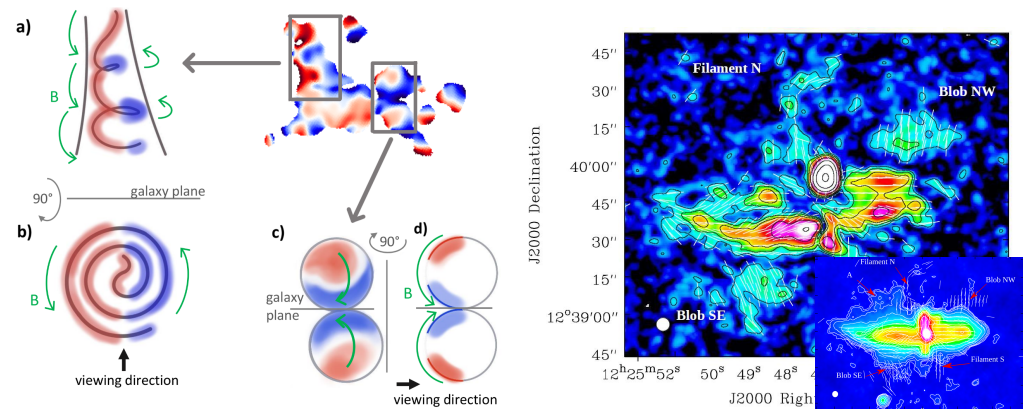


**Figure 10.** In the left image, we see RM patterns of NGC 4217. The RM image (upper right) shows two boxes which highlight a feature extending almost 7 kpc into the halo (left box) and two bubble-like features (right box). Models showing a helical field (top left, labelled **a**) and circumferential field (bottom right, labelled **c** and **d**) correspond to the two boxes, respectively. A possible orientation of the in-disk field is shown on the lower left (labelled **b**). From [19]. In the right image, the galaxy NGC 4388 shows complex structure in polarization intensity (PI). Lower inset: Total intensity emission; the marked difference compared to PI should be noted. From [66].

#### 3.4.4. Large-Scale Regular Magnetic Field Patterns in Galaxy Disks

Reversing RM patterns have now been observed in the *disks* of all CHANG-ES galaxies for which RM analysis could be carried out [29]. The RM data of NGC 4013 and NGC 4217, in particular, show sign changes from the western to the eastern half to the disk [9,52]. This indicates a large-scale regular field with a dominating azimuthal component, like an axisymmetric spiral field with a small pitch angle, as also observed in face-on galaxies [58]. By comparing the sign of RM with the sign of the galaxy rotation and assuming trailing spirals, the radial field component is found to point outwards in NGC 4013, but inwards in NGC 4217.

The first external galaxy in which field reversals were observed along the disk itself was the CHANG-ES galaxy, NGC 4666 [9]. This phenomenon resembles the radial field reversal found in the Milky Way [68], so our Galaxy is no longer a special case. The radial field in NGC 4666 points inwards in the inner part of the disk within a 4 kpc radius, but outwards in the outer disk at 4–9 kpc radius.

#### 3.5. The Observational Three-Dimensional Magnetized Galaxy

Galaxies are complex three-dimensional objects. With the edge-on perspective of the CHANG-ES project, we perfectly see the extended radio halo, while the disk appears strongly compressed. The structure of disks in the radio emission needs to be investigated in moderately inclined galaxies. Then, by combining the two views, we can get the full story.

In almost face-on or weakly inclined spiral galaxies, unpolarized synchrotron emissions (tracing isotropic turbulent fields) are the strongest in spiral arms and bars (20–30  $\mu\text{G}$ ) and in central starburst regions (50–100  $\mu\text{G}$ ). Polarized emissions (tracing ordered fields, which can be regular or anisotropic turbulent, Section 3.4) are generally strongest in inter-arm regions (10–15  $\mu\text{G}$ ). In several galaxies, “magnetic arms” between gaseous spiral arms were observed. In galaxies with strong density waves, ordered fields were observed at the inner edges of spiral arms [57].

Faraday rotation measures (RMs) of the diffuse polarized radio emission from galaxy disks reveal large-scale patterns that can be described by a superposition of azimuthal modes. The lowest dynamo mode is an axisymmetric spiral field and dominates in many galaxies [58] (e.g., in M 31), consistent with the reversing RM signs in both halves of the disk of some edge-on galaxies (Section 3.4.4). Magnetic modes are thought to be signatures of regular fields generated by the large-scale (mean-field) dynamo (see Section 3.6). According

to the RM data of two galaxies (so far) (NGC 628 and IC 342), helically twisted field loops wind around spiral arms [57].

On kpc scales, RM patterns with reversing signs were observed, e.g., in M 51 [69]. These may be attributed to magnetic Parker loops or to local outflows into the halo, possibly related to the “magnetic ropes” in NGC 4631 [65].

We need to understand to what extent the observed patterns are underlying and possibly common to galaxies as part of the regular, dynamo-generated field, and to what extent they may be ‘local’ or galaxy-specific, such as relating to individual spiral arms, SFRs, or specific outflow features (e.g., Figure 10). In the next section, we will focus on theoretical expectations from dynamo theory.

### 3.6. The Theoretical Three-Dimensional Magnetized Galaxy

It is clear that large-scale magnetic spiral structures exist in many nearly face-on spirals, e.g., [64]. On smaller scales, there is a turbulent field component, and total magnetic field strengths are often of the order of  $10 \mu\text{G}$  (Section 3.5). There is a strong indication from edge-on galaxies, known for some time now, that magnetic fields exist in galactic halos as seen in the famous “X fields” [55], and Section 3.4, which introduced some theoretical work from, for example, refs. [70,71]. The origin of these fields has been attributed to classical dynamo action, comprised of sub-scale ( $\lesssim 100 \text{ pc}$ ) turbulence, together with macroscopic ionized gas flows such as rotation and winds. The implications of the dynamo theory are complex and the classical theory itself is not entirely satisfactory. This led to various variations and approximations of the equations, while attempting to explain, especially, the magnetic spirals. Much of this work is summarized, with references, in [72]. The X fields, in particular, have now been detected via the composite picture from CHANG-ES (Figure 6 left) for the set of 28 edge-on galaxies. This confirms their widespread presence and points to a common, rather than galaxy-specific, origin. Moreover, large-scale magnetic fields in CHANG-ES galaxies appear to be robust and not easily destroyed. For example, a number of CHANG-ES galaxies have close companions, or are in clusters, yet they still have large-scale fields [29].

Perhaps the most novel result of the CHANG-ES campaign was the detection of oscillating, line of sight, magnetic fields in galactic halos and disks (Sections 3.4.3 and 3.4.4). Such patterns are ‘universal’ in the CHANG-ES sample. Although novel, this was not entirely unexpected, due to an earlier theoretical treatment. This was predicted by a steady-state model using a version of the classical dynamo equations [62]. In this and subsequent papers, the galactic magnetic field was assumed to be a scale invariant system from the turbulent regime to the halo in the classical picture. This general assumption allowed for a consistent value for the  $\alpha$  effect, the macroscopic velocities and the mean magnetic field. There was ultimately no limitation on the field geometry, although this first paper dealt only with small pitch angles. Nevertheless the planar magnetic spirals and the oscillating fields in the halo were already predicted. The theoretical conclusion was that the magnetic spiral arms and the X fields could be related and explained, by a model of magnetic fields spiraling about the galactic axis and rising into the halo from the plane of the galaxy. This is the first time that X-shaped fields, as well as reversing-sign RM patterns, have both been modeled.

The justification for this master assumption of scale invariance was partly to produce an internally consistent solvable model. However, it is known that complex, self-interacting, and isolated systems do tend to become scale invariant over a finite range of scales. This is the inertial range in hydrodynamic turbulence, and, indeed, any self-similar fractal structure illustrates this. The program was carried on to become exact, time dependent (a reasonable growth rate, including exponential, follows) with many illustrative examples [73]. The examples illustrated various parts of the global dynamo. For example, outflow from the galaxy, together with rotation, were key amplifiers once a seed field was produced. The outflow avoided the saturation expected for a finite dynamo.

The research effort culminated in a detailed attempt [74] to summarize and match the observed halo results for NGC 4631, shown in Figure 9. This paper gives the mature scale invariant theory and its application to the halo of NGC4631. A typical result is shown in Figure 11. The three-dimensional magnetic fields also have strong poloidal components that appear to loop over the projected spirals near the disk (similar to NGC 628 and IC 342, Section 3.5). The results suggest that the ‘magnetic ropes’ discussed in Section 3.4.3 may be part of an even larger scale dynamo-generated structure. The Milky Way has also been found to have changes in magnetic helicity crossing the disc [75], based on the theoretical models that were used to describe CHANG-ES data; the spiraling magnetic fields agreed well with the empirical model of the Milky Way magnetic field.

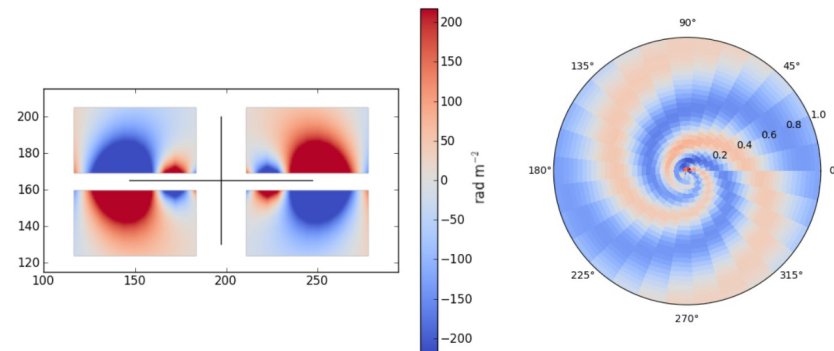


**Figure 11.** One model from [74] from a fit to NGC 4631, which includes outflow. On the left, reversing RMs are seen from an edge-on perspective. On the right, magnetic spirals continue from the disk to the halo. One slice at  $z = 0$  is shown from a face-on perspective.

The CHANG-ES campaign inspired a new look at the magnetic field of galaxies. In many cases, it is clear that the field has an effect on gas motions generally and vice versa. The models agree with observations, and are consistent with extending the scale invariance to even larger scales, that is, the galactic magnetic field may well be connected to the intergalactic plasma. Cluster magnetic fields may then rely on a form of sub-scale turbulence [76,77] produced by galactic motions.

#### 4. Ongoing Activities and New Opportunities

##### 4.1. The S-Band CHANG-ES Extension—Filling the Gap

S-band data, which fill in the gap between L-band and C-band (shown in green in Figure 2) have now been collected for all CHANG-ES galaxies. As illustrated, the new frequency coverage (L-band, S-band, and C-band) is almost contiguous from 1.25 to 7.02 GHz, and provides an unprecedented opportunity to study the spatially resolved spectral index in galaxies. Polarization studies will especially benefit from the addition of S-band data. Currently, polarization analyses are still very limited because L-band data suffer from strong depolarization and rotation (Figure 6, right), and C-band data have too low a resolution in Faraday space.

When combining all radio data, CHANG-ES provides unprecedented frequency coverage for a complete sample of well-resolved edge-on spiral galaxies. Significant results have been obtained from the individual frequency bands, as described in previous sections, but the analysis of the complete frequency range has yet to begin. This includes spectral index structure, including the radio spectrum in the separation of thermal and nonthermal emissions, spectral curvature, and Faraday tomography [59] (see Section 4.2) of the diffuse emission and background sources.

S-band data analysis is currently ongoing, but Figure 12 shows some early S-band results for the galaxy NGC 3044. On the left is a color image of the S-band total intensity superimposed with X-ray XMM contours, and on the right are magnetic field orientations from combined C-band and S-band data superimposed on an  $H\alpha$  map. The contrast



between the thin star-forming disk and the enormous magnetized halo in this galaxy should be noted.

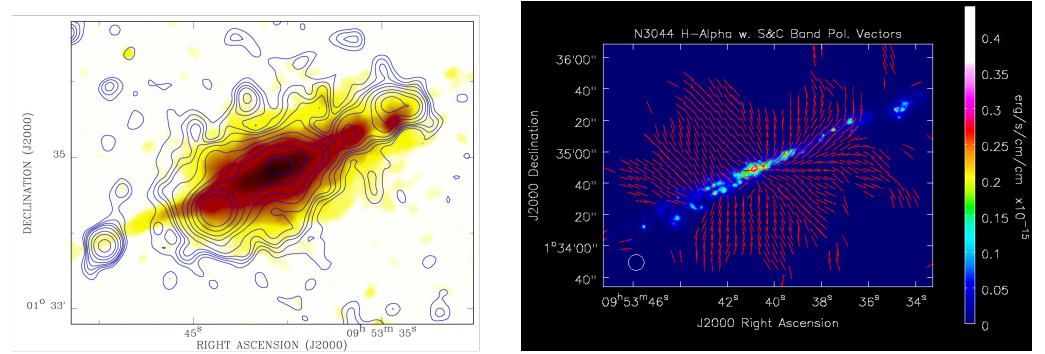


**Figure 12.** NGC 3044 images that include S-band data. On the left, *XMM-Newton* 0.3–1.2 keV intensity contours superimposed on the VLA S-band total intensity image in color. On the right, magnetic field orientations from combined S-band and C-band data superimposed on an  $H\alpha$  image of NGC 3044, from [56].

#### 4.2. Faraday Tomography of Edge-on Galaxies

The large frequency range of the three bands, interrupted only by frequencies lost to RFI will reduce the errors and, therefore, allow more detail to emerge than any single band is able to reveal. Since the images of the sources are resolved, we can investigate both the polarization (obtaining  $B_{\perp}$ ), as well as Faraday analysis (obtaining  $B_{\parallel}$ ), to reconstruct the three-dimensional structure of the magnetic field in the source. This is called *Faraday tomography*, and it has the potential to vividly expose the magnetic field in unprecedented detail (see also Section 3.4 for an overview and explanation of terms).

Faraday tomography is sensitive to structures with a Faraday depth width of up to  $1700 \text{ rad m}^{-2}$  at a resolution of  $40 \text{ rad m}^{-2}$ . At this resolution, the expected error in the rotation measure for a signal-to-noise ratio of 7 in polarized intensity is  $\sim 3 \text{ rad m}^{-2}$ . This will allow the mapping of the structure of the halo in Faraday depth space for both Faraday thin and Faraday thick components.

Heald et al. [78] presented the Faraday rotation measure Synthesis for a sample of galaxies from the SINGS survey with various inclinations, covering two bands in the frequency range 1300 to 1763 MHz. These data revealed complex Faraday rotation and depolarization in the halos of galaxies. The CHANG-ES survey, by contrast, provides frequency coverage from 1 GHz to 7 GHz.

The separation of lines of sight through the halo versus lines of sight through the disk in edge-on galaxies is of special importance for Faraday tomography of the halo and the disk-halo interface. Images of polarized intensity tend to show polarized emissions from the halo while the disk midplane is depolarized (e.g., Figure 7). For (nearly) continuous frequency coverage between 1 GHz and 7 GHz, the largest continuous Faraday depth range, which is limited by differential Faraday rotation along the line of sight, is  $1.7 \times 10^3 \text{ rad m}^{-2}$ . This is more than double the mean Faraday rotation in most of the Milky Way disk, so differential Faraday rotation along the line of sight should pose no significant limitations for probing the halo and most of the disk with diffuse polarization.

We intend to apply frequency averaging to a maximum Faraday depth  $\pm 2500 \text{ rad m}^{-2}$  as a compromise between imaging constraints, including effective cleaning of the Stokes Q and U images, and sensitivity to extreme Faraday rotation. The resolution in Faraday depth, using all three bands, is  $\simeq 40 \text{ rad m}^{-2}$ , depending on frequencies lost to RFI. This resolution corresponds to Faraday rotation over a path length

$$\ell_{\Delta\phi} = 10^2 \left( \frac{n_e}{0.1 \text{ cm}^{-3}} \right)^{-1} \left( \frac{B_{\parallel}}{5 \mu\text{G}} \right)^{-1} \text{ pc.} \quad (4)$$



The Faraday depth resolution of the combined L/S/C band data should, therefore, be sufficient to differentiate between emissions of successive spiral arms along the line of sight close to the disk. In the halo, the high Faraday depth resolution is the most important parameter to reduce measurement errors for RM, thus revealing subtle differences in Faraday rotation in the halo.

An angular resolution of  $10''$  corresponds to a scale,  $484 (d/10 \text{ Mpc}) \text{ pc}$ . This is a factor of 5–10 larger than the outer scale for energy injection of turbulence in the interstellar medium. Differential Faraday rotation within the beam is to be expected, leading to modest Faraday complexity. Also, magnetic field structures smaller than the beam lead to wavelength-independent depolarization, most likely in the disk.

#### 4.3. Toward Understanding Galactic Ecosystems of Star-Forming Galaxies

CHANG-ES data have now provided a solid foundation for furthering our understanding of the Circumgalactic Medium (CGM), a key part of the dynamic galactic ecosystem. The ordered magnetic field typically extends far out from the galactic disk into the halo, as illustrated in Figure 1. The extraplanar radio emissions are prominent in total and polarized intensities and sometimes show loop or shell-like structures, apparently representing blowout superbubbles (Figure 10). In some cases, such structures have multi-wavelength counterparts, observed as  $H\alpha$  and optical dust filaments, as well as in the diffuse X-ray emissions, which show similar overall morphologies [19]. Moreover, winds are implied for most galaxies (Section 3.3.1). All of these features suggest an active and dynamic connection between the galaxy and CGM.

Existing studies of CHANG-ES galaxies are largely based on the initial VLA L- and C-band survey data. The inclusion of S-band data (Section 4.1), as well as single-dish observations (Section 4.5), will lead to profound insights into the magnetic halos of galaxies, as preliminary analysis of the S-band pilot observations has shown (Figure 12). With S-band, we expect to see even more spectacular halo features in both total intensity and polarized emissions.

The radio emission traces the CR electrons and magnetic fields, which are an important energetic component of the CGM. Another energetic component is the diffuse hot plasma produced by similar galactic feedback (AGNs, massive stellar winds, and SNe). Indeed, the diffuse soft X-ray emission generally shows a global similarity with the radio emission (Figure 12 left), although there is no clear detailed correlation between the two emissions. Therefore, the physical relationship between these two components is still unclear. It is time for a fresh and systematic look at the energetic CGM, taking advantage of the accumulation of complementary X-ray data sets and radio observations, to confront evolving theories and simulations.

#### 4.4. Ongoing CHANG-ES Companion Projects—Probing Deeper Into the Galaxies and Exploring the Multi-Phase CGM

In addition to its major science related to the radio continuum observations, CHANG-ES also has a few companion multi-wavelength observational projects, studying different phases of the galaxies and CGM, as described in this section.

The CHANG-ES VLA L-band data cover the HI 21 cm line, as pointed out in Section 2.3. Although the observational design was not optimized for emission line studies, these HI data were nevertheless successfully extracted and published in [30,79] (see also Table 2), revealing high-resolution images of the cold atomic gas. Furthermore, many CHANG-ES galaxies have also been observed in X-ray [80], IR [6], and  $H\alpha$  imaging [5], probing different CGM phases in and around the galaxies.

The CHANG-ES consortium has also initiated two companion projects studying the cold molecular gas via CO emission lines observed with the IRAM (Institute for Radio Astronomy in the Millimetre Range) 30 m telescope (called the ‘CO-CHANGES’ project [81,82]), and the extraplanar diffuse ionized gas (eDIG) observed in a special multi-slit narrow-band spectroscopy mode with the MDM (Michigan-Dartmouth-MIT) 2.4 m

telescope (the ‘eDIG-CHANGES’ project [83,84]). As examples, in Figure 13, we show the distribution of the cold molecular and atomic gas mass of the CO-CHANGES sample (left) and an example of our multi-slit narrow-band spectroscopy observations of the CHANG-ES galaxy NGC 3556 (right). The spectroscopy data from these two projects can be used to study the dynamics of the molecular and ionized gas of CHANG-ES galaxies. In Figure 13 (right), we present a pilot comparison of the position-velocity (PV) diagram of these two gas phases extracted from the midplane of NGC 3556 [83]. Apparently, these two gas phases follow the same dynamics, which should be dominated by the global rotation of the galaxy. Combined with the study of the CR electrons and magnetic fields from the radio continuum data, these CHANG-ES companion projects will help us to have a panchromatic view of the role of different gas phases in galaxy evolution.

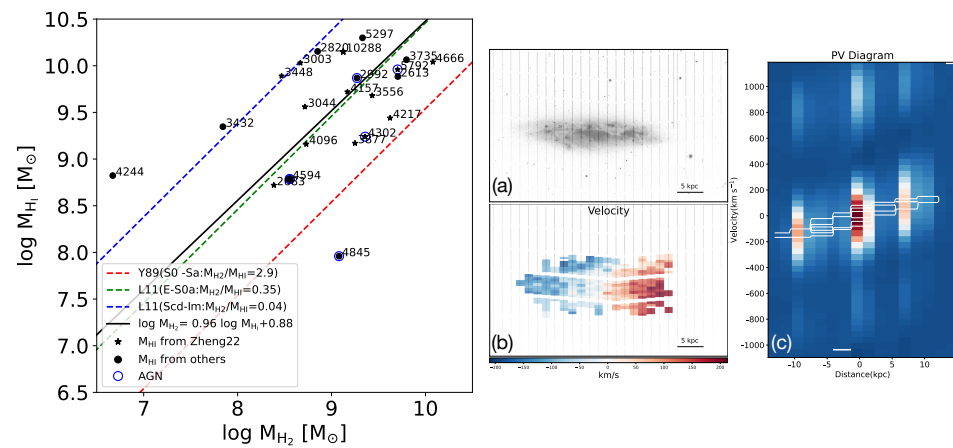


**Figure 13.** On the left, (single frame) molecular gas mass measured with the IRAM 30m observations from the CO-CHANGES project vs. atomic gas mass collected from the archive [81]. Best-fit relations from different literature sources are plotted in colored lines for comparison, with the black solid line the best-fit of the CO-CHANGES sample. On the right (three frames labelled (a–c)), a pilot study of NGC 3556 from the eDIG-CHANGES project [83]: (a) The multi-slit mask overlaid on a snapshot H $\alpha$  image of NGC 3556. Each slit produces a narrow-band spectrum covering the H $\alpha$  line and [N II] $\lambda\lambda$ 6548, 6583 doublet. (b) The line centroid velocity map showing clear rotating disk structures. (c) PV diagram extracted from the midplane of the galaxy. The three parallel bright bands separated in the velocity space are the H $\alpha$  line (middle) and the two [N II] lines. The contours are the CO  $J = 1 - 0$  PV diagram constructed with our IRAM 30 m data [81]. PV diagrams of the two gas phases have comparable slopes, indicating that they follow similar dynamics.

#### 4.5. Green Bank Telescope (GBT) Observations and Joint VLA-GBT Deconvolution

The CHANG-ES sample was observed with the GBT with the purpose of correcting VLA images for missing short-spacing flux via joint deconvolution, based on the method of [85] which incorporates wideband multi-frequency synthesis and multi-scale and mosaic imaging. Optimization of the joint deconvolution is a remaining goal.

#### 4.6. Lagging Extraplanar Gas and Nonthermal Radial Pressure Gradients

Studies of the kinematics of extraplanar atomic and diffuse ionized gas show that rotation speed drops with height above the plane in many galaxies at a rate that, so far, has defied explanation. A certain extraplanar rotational lag is predicted by considering a ballistic model of disk–halo circulation [86,87], but many lags exceed this prediction substantially, e.g., ref. [88]. One class of explanations involves the mixing of disk–halo cycled and primordial infalling gas of much lower angular momentum [89]. Another class notes that the vertical density gradient of extraplanar gas means that any radial pressure gradients that might exist will cause a greater acceleration with height from the plane [90]. Specifically, low density extraplanar gas may be supported by a radially declining pressure

with a rotation speed lower than expected in the ballistic case. The pressure is most likely nonthermal or due to hot gas.

The nonthermal radial pressure gradient can be inferred from CHANG-ES VLA, or eventually VLA-GBT, maps of galaxies with a sufficiently bright extraplanar emission using the equipartition assumption and an adaptation of tilted-ring modeling. Together, simple axisymmetric 3D models of the total magnetic field strength can be fit to the major-axis emission profile in C- or L-band at different heights, from which the pressure gradients can be derived [91]. This is a remaining goal of the project. The technique can also provide an independent way of measuring magnetic field scale-heights and vertical nonthermal pressure gradients.

## 5. Summary and Open Questions

CHANG-ES has presented a unique view of edge-on galaxies using VLA data in wide L- and C-bands. Together with polarization data, the project has confirmed some previously known phenomena, expanded our knowledge of others, and revealed entirely new phenomena never before seen in any galaxy, as summarized below. The wide bandwidths of the VLA have provided opportunities to expand how we deal with spectral indices, and we have developed new techniques in imaging to produce spectacular images of galaxy halos (Figure 1).

We now know that AGNs or low-luminosity AGNs are embedded in at least 64% of a sample of 33 galaxies, even though AGNs were not targeted by any selection criteria. AGNs had previously been detected in some galaxies, but are new discoveries in others. A new time-variable source, new bipolar structures, and a new AGN-related activity revealed by polarization are examples. Circular polarization has also been detected for the first time in the cores of some CHANG-ES galaxies (Section 3.1). Discrete sources with their X-ray counterparts have been cataloged and an active binary star system was identified (Section 3.2).

The largest halos correspond to the largest galaxies, suggesting a ‘scalability’ to these systems. Disk–halo scale-heights have been measured, as well as frequency-dependent spectral indices (Section 3.3). This information, together with the SPINNAKER model, have determined whether the CR transport is diffusion-dominated or advection-dominated. Most galaxies are advection-dominated, implying that most CHANG-ES galaxies experience winds, some of which exceed the escape velocity (Table 3). Just like the solar wind, however, escape may be dictated by magnetic forces rather than gravitational ones [92]. It is not yet clear to what extent the galaxies are calorimeters, nor is it clear why the slope of the radio versus SFR plot is superlinear (Section 3.3.2). More comprehensive measurements of mass-loss rates (e.g., as in [49]) are needed.

The polarization results from CHANG-ES (Section 3.4) have been some of the most stunning. These include galaxy-specific loops, bubbles, and outflow features (e.g., Figure 10), as well as features that appear to be more constant from galaxy to galaxy. Large-scale magnetic field patterns appear to be stable, even in the presence of close companions or cluster members. These patterns include X-type fields in the plane of the sky (Figure 6 left), stronger polarization on the advancing side of the galaxy (Section 3.4.2), as well as alternating RM patterns that imply reversing magnetic field directions in the line of sight (Figure 9, and Figure 7, right). Reversing B field directions are new phenomena never before seen in an external galaxy. We have shown that this behavior, as well as X-type fields in the plane of the sky, are common in galaxies. One explanation requires spiral structures with Faraday depth effects (Sections 3.4.3 and 3.4.4). Such patterns, however, are also predicted from dynamo theory (Section 3.6, Figure 11), which can produce a variety of spiral modes. What, then, determines which modes will be dominant? B fields are generated by dynamos acting on sub-scale turbulence, combined with macroscopic motions (rotation, outflows), but to what extent does SFR-related activity deform these fields on large scales? Future S-band data with magnetic field tomography (Section 4.2) studies can help to disentangle these

effects. More sensitive data may also help to answer the following questions: Where do the large-scale field lines connect? Do they loop around the galaxy, or connect to the IGM field?

The CHANG-ES consortium is open to collaboration (please contact the first author, if interested). FITS images, as outlined in Table 2, are available for general use.

**Author Contributions:** Conceptualization, J.I. and J.-T.L.; Methodology, J.E., V.H., E.M., J.S., A.S. and R.W.; Software, V.H. and R.H.; Validation, T.W.; Formal analysis, J.I., R.B., T.C., R.-J.D., J.E., V.H., R.H., Y.J., J.-T.L., L.-Y.L., C.M., A.M., R.R., N.S., M.S., Y.S., J.S., R.W., Q.D.W., T.W. and Y.Y.; Investigation, T.P. and A.S.; Writing—original draft, J.I., R.B., R.-J.D., J.E., V.H., R.H., J.-T.L., R.R., J.S., A.S., R.W. and Q.D.W.; Writing—review and editing, A.M.; Supervision, J.I., R.-J.D. and J.-T.L.; Project administration, J.I. All authors have read and agreed to the published version of the manuscript.

**Funding:** This research was funded by the Natural Sciences and Engineering Research Council of Canada, Discovery Grant RGPIN-02456 to the first author. RJD, CM, and MS acknowledge funding from the German Research Foundation DFG, within the Collaborative Research Center SFB1491 “Cosmic Interacting Matters—From Source to Signal”. TW acknowledges financial support from the grant CEX2021-001131-S funded by MICIU/AEI/ 10.13039/501100011033, from the coordination of the participation in SKA-SPAIN, funded by the Ministry of Science, Innovation and Universities (MICIU).

**Data Availability Statement:** Data is contained within the article.

**Acknowledgments:** The authors wish to thank their respective funding agencies. Thanks also to MDPI and anonymous referees and editors.

**Conflicts of Interest:** The authors declare no conflicts of interest.

## Notes

- <sup>1</sup> Formerly known as the Expanded Very Large Array, or EVLA.
- <sup>2</sup> A charming 3-minute video for the technically minded can be found at <https://www.youtube.com/watch?v=jwMfNKEsCmE> (accessed on 4 May 2024)
- <sup>3</sup> Data reduction uses the Common Astronomy Software Applications (CASA) package at <http://casa.nrao.edu> (accessed on 4 May 2024) which employs these sophisticated algorithms.
- <sup>4</sup> [https://projects.canfar.net/changes/wp-content/uploads/2019/04/N3079\\_B8.jpg](https://projects.canfar.net/changes/wp-content/uploads/2019/04/N3079_B8.jpg) (accessed on 4 May 2024)
- <sup>5</sup> The deprecated website was <https://queensu.ca/changes>.
- <sup>6</sup> The normalization, however, is different because of the extra extinction in edge-on galaxies.
- <sup>7</sup> RM, more technically, is defined as the slope of the  $\Phi$  versus  $\lambda^2$  plot [14]. It has the same value as  $FD$  only in simple cases where there is only one Faraday-thin source along the line of sight [59].
- <sup>8</sup> This was the very faint galaxy NGC 4244.

## References

1. Irwin, J.; Damas-Segovia, A.; Krause, M.; Miskolczi, A.; Li, J.; Stein, Y.; English, J.; Henriksen, R.; Beck, R.; Wiegert, T.; et al. CHANG-ES: XVIII—The CHANG-ES Survey and Selected Results. *Galaxies* **2019**, *7*, 42. [CrossRef]
2. Tully, R.B. *Nearby Galaxies Catalog*; Cambridge University Press: Cambridge, UK, 1988.
3. Li, J.T.; Beck, R.; Dettmar, R.J.; Heald, G.; Irwin, J.; Johnson, M.; Kepley, A.A.; Krause, M.; Murphy, E.J.; Orlando, E.; et al. CHANG-ES—VI. Probing Supernova energy deposition in spiral galaxies through multiwavelength relationships. *Mon. Not. R. Astron. Soc.* **2016**, *456*, 1723–1738. [CrossRef]
4. Wiegert, T.; Irwin, J.; Miskolczi, A.; Schmidt, P.; Mora, S.C.; Damas-Segovia, A.; Stein, Y.; English, J.; Rand, R.J.; Santistevan, I.; et al. CHANG-ES. IV. Radio Continuum Emission of 35 Edge-on Galaxies Observed with the Karl G. Jansky Very Large Array in D Configuration—Data Release 1. *Astron. J.* **2015**, *150*, 81. [CrossRef]
5. Vargas, C.J.; Walterbos, R.A.M.; Rand, R.J.; Stil, J.; Krause, M.; Li, J.T.; Irwin, J.; Dettmar, R.J. CHANG-ES. XVII.  $H\alpha$  Imaging of Nearby Edge-on Galaxies, New SFRs, and an Extreme Star Formation Region—Data Release 2. *Astrophys. J.* **2019**, *881*, 26. [CrossRef]
6. Vargas, C.J.; Mora-Partiarroyo, S.C.; Schmidt, P.; Rand, R.J.; Stein, Y.; Walterbos, R.A.M.; Wang, Q.D.; Basu, A.; Patterson, M.; Kepley, A.; et al. CHANG-ES X: Spatially Resolved Separation of Thermal Contribution from Radio Continuum Emission in Edge-on Galaxies. *Astrophys. J.* **2018**, *853*, 128. [CrossRef]
7. Kouroumpatzakis, K.; Zezas, A.; Maragkoudakis, A.; Willner, S.P.; Bonfini, P.; Ashby, M.L.N.; Sell, P.H.; Jarrett, T.H. The Star Formation Reference Survey—V. The effect of extinction, stellar mass, metallicity, and nuclear activity on star-formation rates based on  $H\alpha$  emission. *Mon. Not. R. Astron. Soc.* **2021**, *506*, 3079–3097. [CrossRef]



8. English, J. The Yin and Yang of the Visible and Invisible in Spiral Galaxies. 2021. Available online: <https://illuminateduniverse.org/2021/01/27/the-yin-and-yang-of-the-visible-and-invisible-in-spiral-galaxies/> (accessed on 24 January 2024).
9. Stein, Y.; Dettmar, R.J.; Irwin, J.; Beck, R.; Weżgowiec, M.; Miskolczi, A.; Krause, M.; Heesen, V.; Wiegert, T.; Heald, G.; et al. CHANG-ES. XIII. Transport processes and the magnetic fields of NGC 4666: indication of a reversing disk magnetic field. *Astron. Astrophys.* **2019**, *623*, A33. [\[CrossRef\]](#)
10. Silk, J.; Mamon, G.A. The current status of galaxy formation. *Res. Astron. Astrophys.* **2012**, *12*, 917–946. [\[CrossRef\]](#)
11. Irwin, J.; Beck, R.; Benjamin, R.A.; Dettmar, R.J.; English, J.; Heald, G.; Henriksen, R.N.; Johnson, M.; Krause, M.; Li, J.T.; et al. Continuum Halos in Nearby Galaxies: An EVLA Survey (CHANG-ES). I. Introduction to the Survey. *Astron. J* **2012**, *144*, 43. [\[CrossRef\]](#)
12. Sault, R.J.; Wieringa, M.H. Multi-frequency synthesis techniques in radio interferometric imaging. *Astron. Astrophys. Supp.* **1994**, *108*, 585–594.
13. Rau, U.; Cornwell, T.J. A multi-scale multi-frequency deconvolution algorithm for synthesis imaging in radio interferometry. *Astron. Astrophys.* **2011**, *532*, A71. [\[CrossRef\]](#)
14. Brentjens, M.A.; de Bruyn, A.G. Faraday rotation measure synthesis. *Astron. Astrophys.* **2005**, *441*, 1217–1228. :20052990 [\[CrossRef\]](#)
15. Pratley, L.; Johnston-Hollitt, M. Wide-band Rotation Measure Synthesis. *Astrophys. J.* **2020**, *894*, 38. [\[CrossRef\]](#)
16. Irwin, J.A.; Henriksen, R.N.; Krause, M.; Wang, Q.D.; Wiegert, T.; Murphy, E.J.; Heald, G.; Perlman, E. CHANG-ES V: Nuclear Outflow in a Virgo Cluster Spiral after a Tidal Disruption Event. *Astrophys. J.* **2015**, *809*, 172. [\[CrossRef\]](#)
17. Irwin, J.; Beck, R.; Benjamin, R.A.; Dettmar, R.J.; English, J.; Heald, G.; Henriksen, R.N.; Johnson, M.; Krause, M.; Li, J.T.; et al. Continuum Halos in Nearby Galaxies: An EVLA Survey (CHANG-ES). II. First Results on NGC 4631. *Astron. J* **2012**, *144*, 44. [\[CrossRef\]](#)
18. Schmidt, P.; Krause, M.; Heesen, V.; Basu, A.; Beck, R.; Wiegert, T.; Irwin, J.A.; Heald, G.; Rand, R.J.; Li, J.T.; et al. CHANG-ES. XVI. An in-depth view of the cosmic-ray transport in the edge-on spiral galaxies NGC 891 and NGC 4565. *Astron. Astrophys.* **2019**, *632*, A12. [\[CrossRef\]](#)
19. Stein, Y.; Dettmar, R.J.; Beck, R.; Irwin, J.; Wiegert, T.; Miskolczi, A.; Wang, Q.D.; English, J.; Henriksen, R.; Radica, M.; et al. CHANG-ES. XXI. Transport processes and the X-shaped magnetic field of NGC 4217: Off-center superbubble structure. *Astron. Astrophys.* **2020**, *639*, A111. [\[CrossRef\]](#)
20. Tabatabaei, F.S.; Beck, R.; Krügel, E.; Krause, M.; Berkhuijsen, E.M.; Gordon, K.D.; Menten, K.M. High-resolution radio continuum survey of M 33. II. Thermal and nonthermal emission. *Astron. Astrophys.* **2007**, *475*, 133–143. :20078174 [\[CrossRef\]](#)
21. Calzetti, D.; Kennicutt, R.C.; Engelbracht, C.W.; Leitherer, C.; Draine, B.T.; Kewley, L.; Moustakas, J.; Sosey, M.; Dale, D.A.; Gordon, K.D.; et al. The Calibration of Mid-Infrared Star Formation Rate Indicators. *Astrophys. J.* **2007**, *666*, 870–895. [\[CrossRef\]](#)
22. Cabral, B.; Leedom, L.C. Imaging vector fields using line integral convolution. In Proceedings of the 20th annual Conference on Computer Graphics and Interactive Techniques, Anaheim, CA, USA, 2–6 August 1993; ACM: New York, NY, USA, 1993; SIGGRAPH '93, pp. 263–270. [\[CrossRef\]](#)
23. English, J.; Richardson, M.L.A.; Ferrand, G.; Deg, N. CosmosCanvas: Useful Color Maps for Different Astrophysical Properties. Astrophysics Source Code Library. Available online: <https://ascl.net/2401.005> (accessed on 4 May 2024).
24. Irwin, J.; Wiegert, T.; Merritt, A.; Weżgowiec, M.; Hunt, L.; Woodfinden, A.; Stein, Y.; Damas-Segovia, A.; Li, J.; Wang, Q.D.; et al. CHANG-ES. XX. High-resolution Radio Continuum Images of Edge-on Galaxies and Their AGNs: Data Release 3. *Astron. J* **2019**, *158*, 21. [\[CrossRef\]](#)
25. Kluyver, T.; Ragan-Kelley, B.; Pérez, F.; Granger, B.; Bussonnier, M.; Frederic, J.; Kelley, K.; Hamrick, J.; Grout, J.; Corlay, S.; et al. Jupyter Notebooks—A publishing format for reproducible computational workflows. In Proceedings of the Positioning and Power in Academic Publishing: Players, Agents and Agendas, Göttingen, Germany, 7–9 June 2016; Loizides, F., Schmidt, B., Eds.; IOS Press: Amsterdam, The Netherlands, 2016; pp. 87–90. Available online: <https://ebooks.iospress.nl/publication/42900> (accessed on 4 May 2024)
26. GitHub. 2020. Available online: <https://github.com> (accessed on 4 May 2024).
27. Walterbos, R.; et al. [CHANG-ES]. C-Array Data Release. 2025, *in prep.*
28. Merritt, A. Analysis of Radio Spectral Indices in the CHANG-ES Galaxy Sample. Master's Thesis, Queen's University, Kingston, ON, Canada, 2019. Available online: <https://qspace.library.queensu.ca/items/a27d311a-f59b-4fa5-9fa0-6f85a833b627> (accessed on 4 May 2024).
29. Krause, M.; Irwin, J.; Schmidt, P.; Stein, Y.; Miskolczi, A.; Carolina Mora-Partiarroyo, S.; Wiegert, T.; Beck, R.; Stil, J.M.; Heald, G.; et al. CHANG-ES. XXII. Coherent magnetic fields in the halos of spiral galaxies. *Astron. Astrophys.* **2020**, *639*, A112. [\[CrossRef\]](#)
30. Zheng, Y.; Wang, J.; Irwin, J.; English, J.; Ma, Q.; Wang, R.; Wang, K.; Wang, Q.D.; Krause, M.; Randriamampandry, T.H.; et al. CHANG-ES XXV: H I imaging of nearby edge-on galaxies—Data Release 4. *Mon. Not. R. Astron. Soc.* **2022**, *513*, 1329–1353. [\[CrossRef\]](#)
31. Irwin, J.; Dyer, J.; Drake, L.; Wang, Q.D.; Stil, J.; Stein, Y.; English, J.; Wiegert, T. CHANG-ES - XXVII. A radio/X-ray catalogue of compact sources in and around edge-on galaxies. *Mon. Not. R. Astron. Soc.* **2022**, *512*, 5755–5770. [\[CrossRef\]](#)
32. King, A. How big can a black hole grow? *Mon. Not. R. Astron. Soc.* **2016**, *456*, L109–L112. [\[CrossRef\]](#)
33. Sebastian, B.; Kharb, P.; O'Dea, C.P.; Gallimore, J.F.; Baum, S.A. A radio polarimetric study to disentangle AGN activity and star formation in Seyfert galaxies. *Mon. Not. R. Astron. Soc.* **2020**, *499*, 334–354. [\[CrossRef\]](#)



34. Ho, L.C.; Filippenko, A.V.; Sargent, W.L.W. A Search for “Dwarf” Seyfert Nuclei. III. Spectroscopic Parameters and Properties of the Host Galaxies. *Astrophys. J. Suppl.* **1997**, *112*, 315–390. [\[CrossRef\]](#)
35. Ho, L.C. Radiatively Inefficient Accretion in Nearby Galaxies. *Astrophys. J.* **2009**, *699*, 626–637. [\[CrossRef\]](#)
36. Irwin, J.A.; Henriksen, R.N.; Weżgowiec, M.; Damas-Segovia, A.; Wang, Q.D.; Krause, M.; Heald, G.; Dettmar, R.J.; Li, J.T.; Wiegert, T.; et al. CHANG-ES-XI. Circular polarization in the cores of nearby galaxies. *Mon. Not. R. Astron. Soc.* **2018**, *476*, 5057–5074. [\[CrossRef\]](#)
37. Lee, S.W.; Irwin, J.A.; Dettmar, R.J.; Cunningham, C.T.; Golla, G.; Wang, Q.D. NGC 5775: Anatomy of a disk-halo interface. *Astron. Astrophys.* **2001**, *377*, 759–77. [\[CrossRef\]](#)
38. Irwin, J.A.; Schmidt, P.; Damas-Segovia, A.; Beck, R.; English, J.; Heald, G.; Henriksen, R.N.; Krause, M.; Li, J.T.; Rand, R.J.; et al. CHANG-ES-VIII. Uncovering hidden AGN activity in radio polarization. *Mon. Not. R. Astron. Soc.* **2017**, *464*, 1333–1346. [\[CrossRef\]](#)
39. Yang, Y.; Irwin, J.; Li, J.; Wiegert, T.; Wang, Q.D.; Sun, W.; Damas-Segovia, A.; Li, Z.; Shen, Z.; Walterbos, R.A.M.; et al. CHANG-ES. XXIV. First Detection of a Radio Nuclear Ring and Potential LLGN in NGC 5792. *Astrophys. J.* **2022**, *927*, 4. [\[CrossRef\]](#)
40. Heesen, V. The radio continuum perspective on cosmic-ray transport in external galaxies. *Astrophys. Space Sci.* **2021**, *366*, 117. [\[CrossRef\]](#)
41. Allen, R.J.; Baldwin, J.E.; Sancisi, R. Radio continuum observations of the edge-on disc galaxy NGC 891. *Astron. Astrophys.* **1978**, *62*, 397–409.
42. Strong, A.W.; Porter, T.A.; Digel, S.W.; Jóhannesson, G.; Martin, P.; Moskalenko, I.V.; Murphy, E.J.; Orlando, E. Global Cosmic-ray-related Luminosity and Energy Budget of the Milky Way. *Astrophys. J. Lett.* **2010**, *722*, L58–L63. [\[CrossRef\]](#)
43. Heesen, V.; Dettmar, R.J.; Krause, M.; Beck, R.; Stein, Y. Advective and diffusive cosmic ray transport in galactic haloes. *Mon. Not. R. Astron. Soc.* **2016**, *458*, 332–353. [\[CrossRef\]](#)
44. Krause, M.; Irwin, J.; Wiegert, T.; Miskolczi, A.; Damas-Segovia, A.; Beck, R.; Li, J.T.; Heald, G.; Müller, P.; Stein, Y.; et al. CHANG-ES. IX. Radio scale heights and scale lengths of a consistent sample of 13 spiral galaxies seen edge-on and their correlations. *Astron. Astrophys.* **2018**, *611*, A72. [\[CrossRef\]](#)
45. Heesen, V.; Whitler, L.; Schmidt, P.; Miskolczi, A.; Sridhar, S.S.; Horellou, C.; Beck, R.; Gürkan, G.; Scannapieco, E.; Brüggen, M.; et al. Warped diffusive radio halo around the quiescent spiral edge-on galaxy NGC 4565. *Astron. Astrophys.* **2019**, *628*, L3. [\[CrossRef\]](#)
46. Heesen, V.; de Gasperin, F.; Schulz, S.; Basu, A.; Beck, R.; Brüggen, M.; Dettmar, R.J.; Stein, M.; Gajović, L.; Tabatabaei, F.S.; et al. Diffusion of cosmic-ray electrons in M 51 observed with LOFAR at 54 MHz. *Astron. Astrophys.* **2023**, *672*, A21. [\[CrossRef\]](#)
47. Stein, M.; Heesen, V.; Dettmar, R.J.; Stein, Y.; Brüggen, M.; Beck, R.; Adebahr, B.; Wiegert, T.; Vargas, C.J.; Bomans, D.J.; et al. CHANG-ES. XXVI. Insights into cosmic-ray transport from radio halos in edge-on galaxies. *Astron. Astrophys.* **2023**, *670*, A158. [\[CrossRef\]](#)
48. Miskolczi, A.; Heesen, V.; Horellou, C.; Bomans, D.J.; Beck, R.; Heald, G.; Dettmar, R.J.; Blex, S.; Nikiel-Wroczyński, B.; Chyży, K.T.; et al. CHANG-ES XII. A LOFAR and VLA view of the edge-on star-forming galaxy NGC 3556. *Astron. Astrophys.* **2019**, *622*, A9. [\[CrossRef\]](#)
49. Heald, G.H.; Heesen, V.; Sridhar, S.S.; Beck, R.; Bomans, D.J.; Brüggen, M.; Chyży, K.T.; Damas-Segovia, A.; Dettmar, R.J.; English, J.; et al. CHANG-ES XXIII: Influence of a galactic wind in NGC 5775. *Mon. Not. R. Astron. Soc.* **2022**, *509*, 658–684. [\[CrossRef\]](#)
50. Heesen, V.; Rafferty, D.A.; Horneffer, A.; Beck, R.; Basu, A.; Westcott, J.; Hindson, L.; Brinks, E.; Chyży, K.T.; Scaife, A.M.M.; et al. Exploring the making of a galactic wind in the starbursting dwarf irregular galaxy IC 10 with LOFAR. *Mon. Not. R. Astron. Soc.* **2018**, *476*, 1756–1764. [\[CrossRef\]](#)
51. Heesen, V.; Krause, M.; Beck, R.; Adebahr, B.; Bomans, D.J.; Carretti, E.; Dumke, M.; Heald, G.; Irwin, J.; Koribalski, B.S.; et al. Radio haloes in nearby galaxies modelled with 1D cosmic ray transport using SPINNAKER. *Mon. Not. R. Astron. Soc.* **2018**, *476*, 158–183. [\[CrossRef\]](#)
52. Stein, Y.; Dettmar, R.J.; Weżgowiec, M.; Irwin, J.; Beck, R.; Wiegert, T.; Krause, M.; Li, J.T.; Heesen, V.; Miskolczi, A.; et al. CHANG-ES. XIX. Galaxy NGC 4013: A diffusion-dominated radio halo with plane-parallel disk and vertical halo magnetic fields. *Astron. Astrophys.* **2019**, *632*, A13. [\[CrossRef\]](#)
53. Voelk, H.J. The correlation between radio and far-infrared emission for disk galaxies: A calorimeter theory. *Astron. Astrophys.* **1989**, *218*, 67–70.
54. Niklas, S.; Beck, R. A new approach to the radio-far infrared correlation for non-calorimeter galaxies. *Astron. Astrophys.* **1997**, *320*, 54–64.
55. Krause, M. Magnetic Fields and Star Formation in Spiral Galaxies. In *Proceedings of the Revista Mexicana de Astronomía y Astrofísica Conference Series*; Instituto de Astronomía, Universidad Nacional Autónoma de México: Mexico City, Mexico, 2009; Volume 36, pp. 25–29. [\[CrossRef\]](#)
56. Cook, T. New Radio Observations of Edge-on Galaxies, NGC 2683 and NGC 3044. Master’s Thesis, Queen’s University, Kingston, ON, Canada, 2023. Available online: <https://qspace.library.queensu.ca/items/30c1cbec-f2ad-4db2-be02-95c118433054/> (accessed on 4 May 2024).
57. Beck, R. Magnetic fields in spiral galaxies. *Astron. Astrophys. Rev.* **2015**, *24*, 4. [\[CrossRef\]](#)
58. Beck, R.; Chamandy, L.; Elson, E.; Blackman, E.G. Synthesizing Observations and Theory to Understand Galactic Magnetic Fields: Progress and Challenges. *Galaxies* **2019**, *8*, 4. [\[CrossRef\]](#)

59. Takahashi, K. Introduction to Faraday tomography and its future prospects. *Publ. Astron. Soc. Jpn.* **2023**, *75*, S50–S84. [\[CrossRef\]](#)
60. Braun, R.; Heald, G.; Beck, R. The Westerbork SINGS survey. III. Global magnetic field topology. *Astron. Astrophys.* **2010**, *514*, A42. [\[CrossRef\]](#)
61. Soida, M. Can we observe the poloidal magnetic field? In Proceedings of the The Magnetized Plasma in Galaxy Evolution, Kraków, Poland, 27 September–1 October 2004; Chyzy, K.T., Otmianowska-Mazur, K., Soida, M., Dettmar, R.J., Eds.; Jagiellonian University: Cracow, Poland, 2005; pp. 185–190.
62. Henriksen, R.N. Magnetic spiral arms in galaxy haloes. *Mon. Not. R. Astron. Soc.* **2017**, *469*, 4806–4830. [\[CrossRef\]](#)
63. Henriksen, R.N.; Woodfinden, A.; Irwin, J.A. Exact axially symmetric galactic dynamos. *Mon. Not. R. Astron. Soc.* **2018**, *476*, 635–645. [\[CrossRef\]](#)
64. Beck, R.; Brandenburg, A.; Moss, D.; Shukurov, A.; Sokoloff, D. Galactic Magnetism: Recent Developments and Perspectives. *Annu. Rev. Astron. Astrophys.* **1996**, *34*, 155–206. [\[CrossRef\]](#)
65. Mora-Partiarroyo, S.C.; Krause, M.; Basu, A.; Beck, R.; Wiegert, T.; Irwin, J.; Henriksen, R.; Stein, Y.; Vargas, C.J.; Heesen, V.; et al. CHANG-ES. XV. Large-scale magnetic field reversals in the radio halo of NGC 4631. *Astron. Astrophys.* **2019**, *632*, A11. [\[CrossRef\]](#)
66. Damas-Segovia, A.; Beck, R.; Vollmer, B.; Wiegert, T.; Krause, M.; Irwin, J.; Weżgowiec, M.; Li, J.; Dettmar, R.J.; English, J.; et al. CHANG-ES. VII. Magnetic Outflows from the Virgo Cluster Galaxy NGC 4388. *Astrophys. J.* **2016**, *824*, 30. [\[CrossRef\]](#)
67. Damas-Segovia, A.; et al. CHANG-ES XXVIII: Precession of Nuclear Outflows in the Virgo Seyfert Galaxy, NGC 4388. *in prep.*
68. Brown, J.C.; Haverkorn, M.; Gaensler, B.M.; Taylor, A.R.; Bizunok, N.S.; McClure-Griffiths, N.M.; Dickey, J.M.; Green, A.J. Rotation Measures of Extragalactic Sources behind the Southern Galactic Plane: New Insights into the Large-Scale Magnetic Field of the Inner Milky Way. *Astrophys. J.* **2007**, *663*, 258–266. [\[CrossRef\]](#)
69. Kierdorf, M.; Mao, S.A.; Beck, R.; Basu, A.; Fletcher, A.; Horellou, C.; Tabatabaei, F.; Ott, J.; Haverkorn, M. The magnetized disk-halo transition region of M 51. *Astron. Astrophys.* **2020**, *642*, A118. [\[CrossRef\]](#)
70. Brandenburg, A.; Donner, K.J.; Moss, D.; Shukurov, A.; Sokoloff, D.D.; Tuominen, I. Vertical magnetic fields above the discs of spiral galaxies. *Astron. Astrophys.* **1993**, *271*, 36–50.
71. Moss, D.; Sokoloff, D.; Beck, R.; Krause, M. Galactic winds and the symmetry properties of galactic magnetic fields. *Astron. Astrophys.* **2010**, *512*, A61. [\[CrossRef\]](#)
72. Klein, U.; Fletcher, A. *Galactic and Intergalactic Magnetic Fields*; Springer: Heidelberg, Germany, 2015.
73. Henriksen, R.N.; Irwin, J. Turbulent Magnetic Dynamos with Halo Lags, Winds, and Jets. *Astrophys. J.* **2021**, *920*, 133. [\[CrossRef\]](#)
74. Woodfinden, A.; Henriksen, R.N.; Irwin, J.; Mora-Partiarroyo, S.C. Evolving galactic dynamos and fits to the reversing rotation measures in the halo of NGC 4631. *Mon. Not. R. Astron. Soc.* **2019**, *487*, 1498–1516. [\[CrossRef\]](#)
75. West, J.L.; Henriksen, R.N.; Ferrière, K.; Woodfinden, A.; Jaffe, T.; Gaensler, B.M.; Irwin, J.A. Helicity in the large-scale Galactic magnetic field. *Mon. Not. R. Astron. Soc.* **2020**, *499*, 3673–3689. [\[CrossRef\]](#)
76. Brunetti, G.; Lazarian, A. Stochastic reacceleration of relativistic electrons by turbulent reconnection: a mechanism for cluster-scale radio emission? *Mon. Not. R. Astron. Soc.* **2016**, *458*, 2584–2595. [\[CrossRef\]](#)
77. ZuHone, J.A.; Markevitch, M.; Brunetti, G.; Giacintucci, S. Turbulence and Radio Mini-halos in the Sloshing Cores of Galaxy Clusters. *Astrophys. J.* **2013**, *762*, 78. [\[CrossRef\]](#)
78. Heald, G.; Braun, R.; Edmonds, R. The Westerbork SINGS survey. II Polarization, Faraday rotation, and magnetic fields. *Astron. Astrophys.* **2009**, *503*, 409–435. [\[CrossRef\]](#)
79. Zheng, Y.; Wang, J.; Irwin, J.; Daniel Wang, Q.; Li, J.; English, J.; Ma, Q.; Wang, R.; Wang, K.; Krause, M.; et al. H I Vertical Structure of Nearby Edge-on Galaxies from CHANG-ES. *Res. Astron. Astrophys.* **2022**, *22*, 085004. [\[CrossRef\]](#)
80. Li, J.T.; Wang, Q.D. Chandra survey of nearby highly inclined disc galaxies - I. X-ray measurements of galactic coronae. *Mon. Not. R. Astron. Soc.* **2013**, *428*, 2085–2108. [\[CrossRef\]](#)
81. Jiang, Y.; Li, J.T.; Gao, Y.; Bregmany, J.N.; Ji, L.; Jiang, X.; Tan, Q.; Wang, J.; Wang, Q.D.; Yang, Y. CO-CHANGES II: Spatially resolved IRAM 30m CO line observations of 24 nearby edge-on spiral galaxies. 2024. *in prep.*
82. Jiang, Y.; Li, J.T.; Gao, Y.; Bregmany, J.N.; Ji, L.; Jiang, X.; Tan, Q.; Wang, J.; Wang, Q.D.; Yang, Y. CO-CHANGES I: IRAM 30m CO Observations of Molecular Gas in the Sombrero Galaxy. *Mon. Not. R. Astron. Soc.* **2023**, *528*, 4160–4175. [\[CrossRef\]](#)
83. Li, J.T.; Lu, L.Y.; Qu, Z.; Benjamin, R.A.; Bregman, J.N.; Dettmar, R.-J.; English, J.; Fang, T.; Irwin, J.A.; Jiang, Y.; et al. eDIG-CHANGES II: Project Design and Initial Results on NGC 3556. *arXiv* **2024**, arXiv:2404.05628.
84. Lu, L.Y.; Li, J.T.; Vargas, C.J.; Fang, T.; Bregman, J.N.; Dettmar, R.J.; Heald, G.H.; Walterbos, R.A.M.; Wang, Q.D.; CHANG-ES M. eDIG-CHANGES III: Multi-slit Spectroscopy of the eDIG around NGC 891. 2024. *in prep.*
85. Rau, U.; Naik, N.; Braun, T. A Joint Deconvolution Algorithm to Combine Single-dish and Interferometer Data for Wideband Multiterm and Mosaic Imaging. *Astron. J.* **2019**, *158*, 3. [\[CrossRef\]](#)
86. Collins, J.A.; Benjamin, R.A.; Rand, R.J. Kinematics of Diffuse Ionized Gas Halos: A Ballistic Model of Halo Rotation. *Astrophys. J.* **2002**, *578*, 98–108. [\[CrossRef\]](#)
87. Fraternali, F.; Binney, J.J. A dynamical model for the extraplanar gas in spiral galaxies. *Mon. Not. R. Astron. Soc.* **2006**, *366*, 449–466. [\[CrossRef\]](#)
88. Zschaechner, L.K.; Rand, R.J. The H I Kinematics of NGC 4013: A Steep and Radially Shallowing Extra-planar Rotational Lag. *Astrophys. J.* **2015**, *808*, 153. [\[CrossRef\]](#)
89. Marinacci, F.; Fraternali, F.; Nipoti, C.; Binney, J.; Ciotti, L.; Londrillo, P. Galactic fountains and the rotation of disc-galaxy coronae. *Mon. Not. R. Astron. Soc.* **2011**, *415*, 1534–1542. [\[CrossRef\]](#)

90. Benjamin, R.A. The Interstellar Disk-Halo Connection: The Rotation of Extra-planar Gas. In *Proceedings of the Seeing through the Dust: The Detection of HI and the Exploration of the ISM in Galaxies*; Taylor, A.R., Landecker, T.L., Willis, A.G., Eds.; Astronomical Society of the Pacific: San Francisco, CA, USA, 2002; Volume 276, p. 201.
91. Braun, T.T.; Rau, U.; Rand, R.J.; Kepley, A. Using VLA/GBT Data Combined with a New Interferometer and Single-Dish Joint Deconvolution Technique to Model Radio Halos of Galaxies. In *Proceedings of the American Astronomical Society Meeting Abstracts #233*, Seattle, WA, USA, 6–10 January 2019; Volume 233, p. 260.04.
92. DeForest, C.E.; Howard, T.A.; McComas, D.J. Inbound Waves in the Solar Corona: A Direct Indicator of Alfvén Surface Location. *Astrophys. J.* **2014**, 787, 124. [[CrossRef](#)]

**Disclaimer/Publisher’s Note:** The statements, opinions and data contained in all publications are solely those of the individual author(s) and contributor(s) and not of MDPI and/or the editor(s). MDPI and/or the editor(s) disclaim responsibility for any injury to people or property resulting from any ideas, methods, instructions or products referred to in the content.